J. Fluid Mech. (2014), *vol.* 739, *pp.* 94–123.
doi:10.1017/jfm.2013.618

Numerical analysis of bluff body wakes under periodic open-loop control

Derwin J. Parkin†, M. C. Thompson and J. Sheridan

Fluids Laboratory for Aeronautical and Industrial Research (FLAIR), Department of Mechanical and Aerospace Engineering, Monash University, Clayton, VIC 3800, Australia

(Received 5 March 2013; revised 28 October 2013; accepted 14 November 2013; first published online 17 December 2013)

Large eddy simulations at $Re = 23\,000$ are used to investigate the drag on a two-dimensional elongated cylinder caused by rear-edge periodic actuation, with particular focus on an optimum open-loop configuration. The 3.64 (length/thickness) aspect-ratio cylinder has a rectangular cross-section with rounded leading corners, representing the two-dimensional cross-section of the now generic *Ahmed*-body geometry. The simulations show that the optimum drag reduction occurs in the forcing Strouhal number range of $0.09 \leqslant St_{act} \leqslant 0.135$, which is approximately half of the Strouhal number corresponding to shedding of von Kármán vortices into the wake for the natural case. This result agrees well with recent experiments of Henning *et al.* (*Active Flow Control*, vol. 95, 2007, pp. 369–390). A thorough transient wake analysis employing dynamic mode decomposition is conducted for all cases, with special attention paid to the Koopman modes of the wake flow and vortex progression downstream. Two modes are found to coexist in all cases, the superimposition of which recovers the majority of features observed in the flow. Symmetric vortex shedding in the near wake, which effectively extends the mean recirculation bubble, is shown to be the major mechanism in lowering the drag. This is associated with opposite-signed vortices reducing the influence of natural vortex shedding, resulting in an increase in the pressure in the near wake, while the characteristic wake antisymmetry returns further downstream. Lower-frequency actuation is shown to create larger near-wake symmetric vortices, which improves the effectiveness of this process.

Key words: drag reduction, instability control, vortex shedding

1. Introduction

The drag experienced by ground vehicles can be substantially reduced through aerodynamically favourable geometric modifications during the design process. However, for the heavy class of ground vehicles, where storage space is paramount (truck-trailers, buses, etc.), the geometric alterations possible are severely limited. Alternative strategies in reducing the drag of such vehicles are therefore being explored, with the area of active flow control showing considerable promise.

The usual goal of bluff body flow control directed at minimizing drag is to manipulate the wake behind the body in such a way that the base pressure is increased.

† Email address for correspondence: dparkin7@gmail.com

Passive solutions such as three-dimensional (3D) geometric modification near the rear separation point on two-dimensional (2D) bluff bodies have proved successful at low Reynolds numbers, with the normally 2D shear layers becoming more 3D and less prone to rolling up to form the characteristic von Kármán vortex street (Tanner (1972), Rodriguez (1991) and Petrusma & Gai (1994)). However, these passive methods are less successful as the Reynolds number is increased and 3D effects such as oblique shedding and vortex dislocation begin to appear at random locations along the span (summarized eloquently in Tombazis & Bearman 1997). Furthermore, away from the ideal conditions of the laboratory, those approaches are unable to deal with external effects such as gusts and high upstream turbulence, which apply in practical situations. Time-periodic 2D forcing reduces the first problem by actively targeting the absolute and convective 2D instabilities in the wake (the Strouhal or shear-layer instabilities), reducing the role of 3D instabilities in the global wake development. The second problem can be tackled with closed-loop control, where real-time measurements of the flow can be actively fed back to actuators controlling their output to modify the downstream flow. While closed-loop control provides the promise of substantial drag reduction, potentially with low levels of actuation, a better understanding of open-loop control methods represents a natural precursor step. This paper explores the performance of an open-loop control approach based on sinusoidal forcing at the rear edges of a 2D elongated cylinder with the same cross-section as a flat-back Ahmed body (Ahmed & Ramm 1984), effectively a simplified 2D model with some broad features of a truck cross-section. Of course, trucks are fully 3D, with geometrical complexity, ground plane proximity and 3D flows including drag-inducing trailing vortices originating close to the trailing-face corners. This paper focuses on one of the wake flow components contributing to variations in the drag, i.e. the rollup of the separating shear layers from the top and bottom edges into large-scale (predominantly 2D) vortices, which form a von Kármán wake.

Pioneering experiments were performed by Bearman (1967), who applied base bleed (steady blowing from the rear face) on a flat-back Ahmed body and found that the drag reduced by a third with a large enough bleed. This effect was not surprising considering his analysis of the base flow, which suggested that the vortex formation length (controlled with splitter plates) was a function of base pressure. Effectively, the substantial base bleed pushes the formation length of the wake vortices further from the rear, increasing the base pressure.

Zero-net-mass-flux (ZNMF) actuation at high frequencies has been successfully employed to delay separation of flow over such shapes as circular cylinders and stalled aerofoils, a thorough summary of which is provided by Glezer (2011). A similar technique has also been successfully applied to heavy vehicles with rear flaps, with ZNMF applied just upstream of the flap delaying separation, allowing for a greater angle of flap to be used and thus minimizing the wake area (Nishri & Wygnanski 1998; Hsu, Hammache & Browand 2002). However, for bluff bodies with fixed blunt-trailing edges (this is unavoidable in many countries, where road regulations do not allow for the installation of rear flaps), this mechanism of drag reduction is clearly not possible.

Henning *et al.* (2007) was the first to attempt ZNMF actuation for a 2D blunt trailing-edge body (with an Ahmed body front). Their goal was to delay the evolution of the wake instability by enhancing the initial symmetry of the wake, and thus raising base pressure. This is achieved by increasing the amplitude of the convective shear-layer instability at the rear top and bottom edges, minimizing the influence of smaller natural perturbations so that the shear layers can resist forming a von Kármán

vortex street. The same authors (Pastoor *et al.* 2008) later explained their rationale for exploring this mechanism of drag reduction in particular, compared with three other active methods of attenuating the wake instability presented (direct opposition control of vortices, high-frequency forcing to diminish large-scale vortex formations, and 3D forcing to break large-scale vortex formations): the synchronous shedding method is the most tunable and cheapest to implement, allowing for the greatest closed-loop potential. In the two papers, they analyse the effectiveness of the technique for Reynolds numbers in the range $23\,000 \leqslant Re_H \leqslant 70\,000$, and in the latter analyse the mechanism further via a vortex model. Here the Reynolds number is defined as $Re_H = U_\infty H/\nu$, where ν is the kinematic viscosity, U_∞ is the corrected free-stream fluid speed and H is the height of the body. The experiments were performed in a wind tunnel, and specifically examined the drag reduction as a function of the actuation Strouhal number given by $St_{act} = f_{act}H/U_\infty$, with f_{act} the applied frequency of the actuation. They found that the drag reduction process was most effective between actuation frequencies of $St_{act} = 0.10$ and $St_{act} = 0.20$, with an optimum close to $St_{act} = 0.15$. The higher actuation frequencies, successful for other shapes as discussed, proved less effective: the vortices at these frequencies are too small and, while still shed synchronously, are unable to attenuate the larger alternating structures in the near wake. While Pastoor *et al.* (2008) features the same set of results as Henning *et al.* (2007), the former appears to have corrected the results for blockage. Thus, in the following comparisons with this body of work, we will make reference to the Pastoor *et al.* (2008) paper.

More recently, Krajnovic & Fernandes (2011) examined the flow using large eddy simulation (LES), with the numerical domain and boundary conditions chosen as close as possible to the physical experiments, in order to try to reproduce the experimental result for a single Strouhal number. They achieved relatively good agreement, and observed the synchronous-shedding mechanism. Chiekh *et al.* (2013) conducted a proper orthogonal decomposition analysis of a similar flow, showing a significant redistribution of the energy among the mean flow and lower order modes takes place. However, the experiments were done at $Re_H = 7100$, and the body had an aspect ratio an order of magnitude larger than that used by the aforementioned studies, yielding a significantly lower boundary layer thickness at separation.

Some goals of this work are to better understand how the forcing influences the flow dynamics in the near wake, leading to increased base pressures, and why it is frequencies lower than the Strouhal frequency that are most effective. The resolved time-dependent numerical simulations capture the velocity and pressure fields as a function of time, and hence can substantially supplement the limited information available from the physical experiments of Pastoor *et al.* (2008) and vortex model analysis of Pastoor *et al.* (2008), providing substantially more insight into the underlying flow physics, such as the modes in the flow (to be analysed through dynamic mode decomposition).

This paper is organized as follows. In § 2 the flow problem is defined and the numerical method is discussed. This is a flow with a fully turbulent wake, although at a reasonably low Reynolds number; even so, considerable effort is expended to ensure that the mesh is sufficiently fine to capture the essential flow physics and the model is capable of quantitative predictions. This is done both through grid resolution studies and comparisons with results from previous experiments and simulations. Following this, in § 3, the results are presented and discussed. A main analysis tool is dynamic mode decomposition, so the theory is briefly reviewed before it is used to explore the differences in the wakes of the high and low drag cases. Drag predictions are

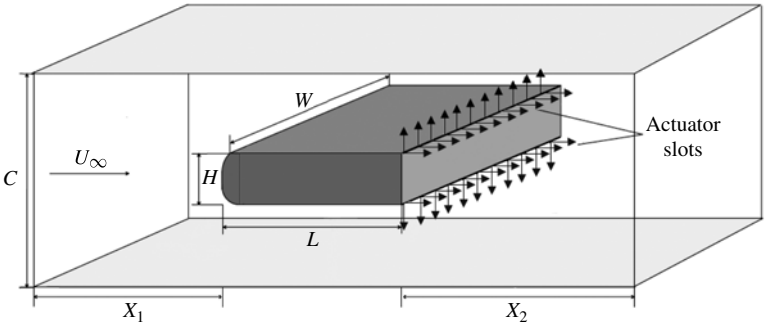

FIGURE 1. Sketch of the 3D flow domain showing the problem setup. The cylinder consists of an elongated rectangle with rounded leading edges, consistent with the Ahmed body geometry. The aspect ratio is $L/H = 3.64$. The computational domain dimensions are $X_1 = 6.61H$, $X_2 = 24.47H$ and $C = 7.71H$. The domain extends into the third dimension by a distance of $W = 1.74H$.

presented and compared with experimental results, and the wake formation length, which is directly related to the drag, is quantified. The paper concludes with a review of the main findings and implications.

2. Methodology

2.1. *Problem definition and computational domain considerations*

The problem setup is shown in figure 1. The body consists of a rectangular cylinder with rounded leading edges, equivalent to a cross-section through an Ahmed body, which has become a standard model geometry to investigate some generic aspects of automobile aerodynamics. The same cross-sectional dimensions and geometry have been used in the experimental study by Pastoor *et al.* (2008) and the numerical study of Krajnovic & Fernandes (2011). For the experiments of Pastoor *et al.* (2008), the body extended across the entire working section of the tunnel, giving a width of $W = 7.64H$. The numerical study of Krajnovic & Fernandes (2011) used the same setup with the cylinder extending to the no-slip computational tunnel walls. The setup here is slightly different, with a free-slip condition applied at all domain boundaries (including the spanwise), in an attempt to reduce the otherwise substantial end effects. Care was taken in setting the spanwise width and the spanwise resolution, to properly capture the spanwise flow scales. To test the influence of the former, the width of model used was progressively halved from a width of $6.96H$ to $0.87H$. The solution differed significantly between the cases $W = 1.74H$ and $W = 0.87H$, but negligible changes were observed for $W \geqslant 1.74$. The final spanwise dimension was therefore chosen as $1.74H$. The details of the spanwise resolution are given in § 2.2.

Apart from this difference, the two previous studies incorporated legs supporting the cylinder, even though it was placed on the centreplane of the tunnel. Finally, they also incorporated tapes just downstream of the leading edges, to trip the boundary layer. As suggested by Krajnovic & Fernandes (2011) and in previous related studies of Cooper (1985), transition was found to occur naturally at $Re = 20\,000$ for this geometry, so tapes were not employed here. It was verified that this was indeed the case.

Whilst Pastoor *et al.* (2008) only applied actuation across the middle section of the rear edges, and this was duplicated by Krajnovic & Fernandes (2011) in their numerical study (as they were attempting to duplicate the experimental setup as closely

as possible), they both recommended actuation across the entire span. The aim here is to model a 2D body without end effects. As such, actuation is applied uniformly across the entire span.

One aim of this study is to quantify the drag reduction as a function of the actuation control parameters to compare to experimental findings. The two governing parameters are the forcing frequency of actuation, St_{act}, and the actuation amplitude, quantified here through the momentum coefficient

$$C_\mu = N_a \frac{S}{H} \frac{u_{act}^2}{U_\infty^2}, \tag{2.1}$$

where N_a is the number of actuators, S is the slot width ($1/72H$ for all slots) and u_{act} is the r.m.s. value of the actuation velocity signal $g(t) = A\sin(2\pi f_{act}t)$ (where A is the actual actuation amplitude). As used by Krajnovic & Fernandes (2011), four slots are employed at the trailing-edge corners: one on the top surface, one on the bottom surface and two on the rear face). Actuation from the upper and lower surface slots is perpendicular to the flow, whilst actuation from the rear face slots is directed parallel to the flow. Ideally the actuation amplitude would be as small as possible, but in practice a moderate amplitude forcing is required to significantly influence the turbulent flow. For the actuation frequency sweep, A is fixed at 2.62 m s^{-1} ($0.53U_\infty$), giving $C_\mu = 0.008$. This is comfortably above the saturation value of 0.006 found by Pastoor *et al.* (2008) above which no further drag reduction was achieved (this is revisited briefly at the conclusion of the discussion section). Pastoor *et al.* (2008) showed minimal Reynolds number effects over the range $Re_H = 23\,000$–$70\,000$. The Reynolds number is therefore chosen to be fixed at $Re_H = 23\,000$, allowing for comparison with the experimental results while requiring the lowest mesh resolution possible.

2.2. *Mesh generation and time step selection*

A key issue with simulations involving actuation is the high ratio of fluid speed to inlet velocity in the narrow actuated regions. Care must therefore be taken to resolve the flow gradients around these areas, in addition to resolving the boundary and shear layers, and the near-wake region, by also concentrating the mesh points near the slots. Furthermore, dimensionless wall element dimensions need to be kept within an acceptable range to produce accurate predictions. The mesh shown in figure 2 was developed in accordance with the dimensionless wall value recommendations of Krajnovic (2009). It consists of 7 600 600 elements and features dimensionless wall values $\Delta x^+ \approx 10$–20, $\Delta y^+ \approx 1$–4, $\Delta z^+ \approx 5$–50. While the effect of the Δy^+ value is well documented, the importance of Δz^+ should not be overlooked. Initial simulations run at a lower spanwise resolution yielded vastly different flow statistics to the higher spanwise resolution case, with stronger 2D vortex shedding and a much higher mean drag coefficient.

A grid resolution study was completed with three different relative mesh sizings for natural flow over the streamlined front nose body (and free-slip boundaries). Table 1 summarizes the change in mean drag force and Strouhal number for each mesh sizing, and gives more information on the resolution in the wake (defined here as the box behind the body encompassing $0 < X/H < 1.4$, $-1 < Y/H < 1$ and $0 < Z/W < 1$), the boundary layer and across the slots. The statistics show that increasing the mesh resolution further would likely have negligible impact on both the Strouhal number and mean drag coefficient returned, and limited impact on the spanwise and time-averaged wake velocity profile.

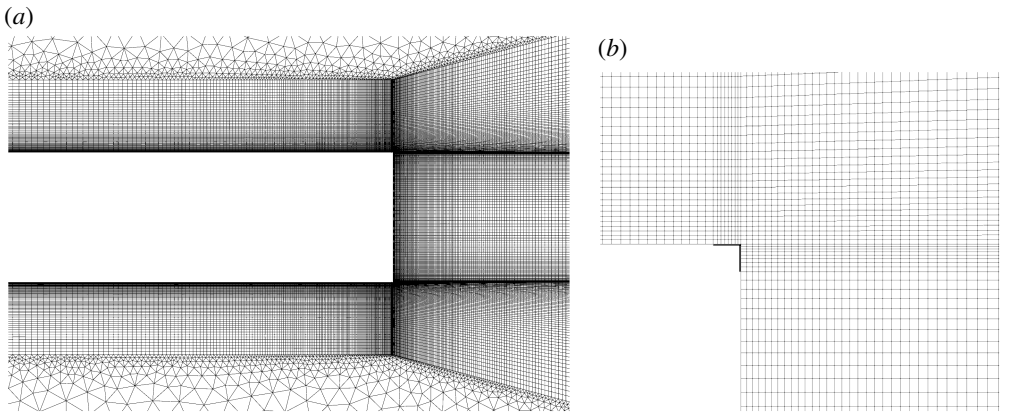

FIGURE 2. (*a*) Cross-section of the mesh in the vicinity of the rear surface. This 2D mesh was swept 70 elements into the spanwise (z) direction. (*b*) Location of the actuator slots near the top right trailing-edge corner and the mesh density in their vicinity. Slots are $1/72H$ wide.

N_{TOTAL}	Wake N	n_x	n_y	n_z	n_{BL}	n_{slot}	$C_{D,0}$	St	$\overline{\epsilon_u}/U_\infty$ (%)	$\overline{\epsilon_v}/U_\infty$ (%)
2 420 000	175 000	72	58	42	22	5	0.60	0.25	1.4	4.9
5 280 000	490 000	96	76	56	34	6	0.72	0.22	0.2	0.1
7 600 000[a]	806 000	120	96	70	44	8	0.72	0.22	—	—

TABLE 1. Predicted mean drag ($C_{D,0}$) and Strouhal number (St) from the grid resolution study for the natural flow. The [a] indicates the final mesh used. All statistics are taken from $t = 1.0$–2.5 s of flow (approximately 100 non-dimensional time units or ∼25 natural shedding cycles). N refers to the number of nodes in a volume, while n refers to the number of nodes across a one-dimensional boundary. n_{BL} refers to the number of mesh rows spanning the boundary layer halfway along the body (calculated *a posteriori*). Here, $\overline{\epsilon_u}/U_\infty$ and $\overline{\epsilon_v}/U_\infty$ refer to the mean error of the streamwise and vertical time-averaged velocity profiles, respectively, at $X = H$ downstream of the rear face. Windowing was not used for the quoted St.

A time step of $\Delta t = 1 \times 10^{-4}$ s was selected: a time step resolution analysis showed that a larger time step of $\Delta t = 2 \times 10^{-4}$ s produced a substantially lower mean drag and lower peaks in the drag spectra, whilst the smaller $\Delta t = 5 \times 10^{-5}$ s showed a very slight decrease in drag (∼1 %) but otherwise negligible changes. The chosen time step gives a non-dimensional time step of 0.0058, which corresponds to approximately 800 time steps per shedding period. Further quantification of this time resolution study are presented in table 2.

The large eddy simulations were run using the element-based finite-volume (FV) commercial code ANSYS CFX based on the standard Smagorinsky subgrid model. Quantities at the face between two control volumes are approximated from nodal values via shape functions for the non-advection terms. For the advection term a blended scheme is used. This uses a weighted combination of a first-order and second-order scheme: when the blend factor (β) is zero the scheme is first-order, and when it is set to one, the scheme is second-order accurate. In this work, as with Krajnovic

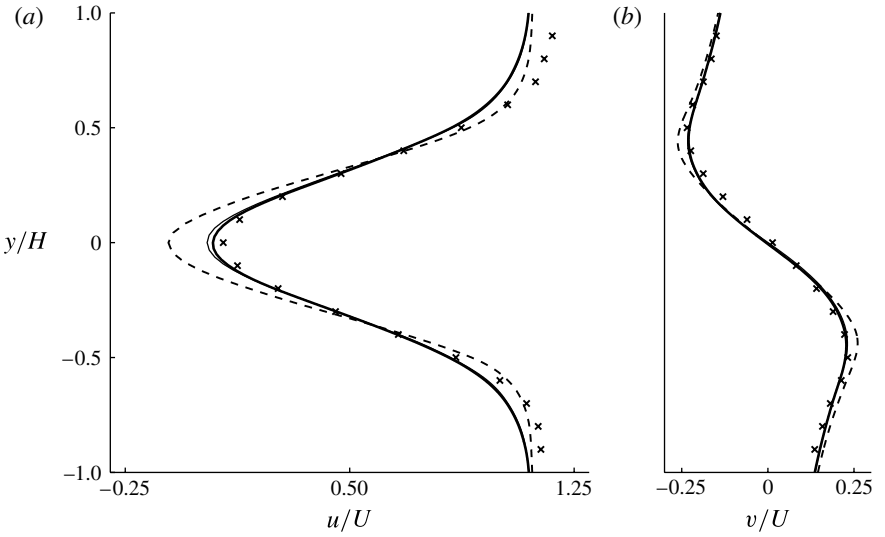

FIGURE 3. Spanwise and time-averaged velocity profiles at $X = H$ downstream of the rear face: (*a*) horizontal velocity and (*b*) vertical velocity. The thick solid line represents the fine mesh (the final mesh used), the thin solid line the medium mesh, and the dashed line the coarse mesh. Crosses represent experimental results of Pastoor *et al.* (2008).

Time step	$C_{D,0}$	St	$\overline{\epsilon_u}/U_\infty$ (%)	$\overline{\epsilon_v}/U_\infty$ (%)
5×10^{-5}	0.71	0.22	—	—
$1 \times 10^{-4}{}^a$	0.72	0.22	0.1	0
2×10^{-4}	0.66	0.23	0.4	0.1

TABLE 2. Predicted mean drag ($C_{D,0}$) and Strouhal number (St) from the time resolution study for the natural flow. The ^{a} indicates the final time step used. These statistics were extracted using approximately 80 non-dimensional time units. Windowing was not used for the quoted St.

& Fernandes (2011), $\beta = 1$ is chosen, returning second-order accuracy in space. The diffusion and pressure gradient terms are also calculated from shape functions, and are second-order.

The second-order (iterative) backward Euler-type scheme was used for temporal discretization.

In line with the standard LES approach, the implicit LES technique in CFX filters out eddies smaller than the grid spacing, resolving the larger structures, which contain the bulk of energy in the flow. However, energy needs to be removed from the resolved scales such that the energy cascade is appropriately mimicked, and this is the job of the subgrid model. The standard Smagorinsky model is an eddy viscosity model, which works on the molecular transport analogy to relate the subgrid stresses to the rate of strain in the fluid via an eddy viscosity ν_t, and they are able to remove an appropriate amount of flow energy with proper case-to-case modification. The Smagorinsky model leans on the assumption that the small scales are in equilibrium and dissipate all energy received from larger scales instantaneously, i.e. there is no

Turbulence model	$C_{D,0}$	St	$P\{St_{act}\}$	$\overline{\epsilon_u}/U_\infty$ (%)	$\overline{\epsilon_v}/U_\infty$ (%)
Smagorinsky[a]	0.72	0.22	—	—	—
Dynamic	0.69	0.23	—	0.7	0.3
Smagorinsky (actuation)[a]	0.62	0.19	0.011	—	—
Dynamic (actuation)	0.60	0.19	0.012	0.7	1.0

TABLE 3. Predicted mean drag ($C_{D,0}$) and Strouhal number (St) for both turbulence models tested. The [a] indicates the final model used. All statistics taken over approximately 80 non-dimensional time units. Actuation case tested: $St_{act} = 0.19$. $P\{St_{act}\}$ is the magnitude of the drag spectra peak at the actuation frequency. Windowing was not used for the quoted St.

back scatter. The eddy viscosity is therefore approximated simply as $\nu_t = (C_s\bar{\Delta})^2|\bar{S}|\bar{S}_{ij}$, where C_s is the specified Smagorinsky coefficient, $\bar{S} \equiv \sqrt{2\bar{S}_{ij}\bar{S}_{ij}}$ (where S_{ij} is the large-scale strain rate tensor) and the grid length $\bar{\Delta}$ is approximated as the cube root of the element volume. C_s was held constant at 0.1, a value leading to moderate damping of the subgrid eddy viscosity dissipation and often used for bluff body flows. This was also used in the Krajnovic & Fernandes (2011) study, and due to good agreement with experimental results (discussed in § 2.3) was chosen as the model for this study. The results for the natural flow case and one actuation case were also compared with the dynamic Smagorinsky model (table 3), which improves on the standard Smagorinsky model by dynamically adjusting C_s using the idea of scale-similarity, which allows the subgrid scales to be modelled from information in the resolved velocity field (Germano *et al.* 1991; Lilly 1992) – although for anisotropic grids and complex geometries, results have been known to vary (Scotti, Meneveau & Fatica 1997). For the natural case the drag coefficient and Strouhal number are within 5 % of the Smagorinsky model values. The velocity profiles also show good agreement, with a slight improvement in the shear-layer regions. Under actuation, a near-identical drag reduction (within 1 %) was returned compared with the standard Smagorinsky case, with differences in wake velocity profiles also negligible. The similar performance of the two models is most likely due to the C_s of 0.1 chosen for the Smagorinsky model: for the dynamic model, the mean C_s values in the shear layers were also around 0.1. It also appears that under actuation, where the flow is artificially regulated in the shear regions, the differences between the models appear to be minimized. These *a posteriori* comparisons, along with the original validation against experimental data, indicate that the Smagorinsky model is an acceptable choice, but also show that the dynamic model is capable of replicating the experimental results well for this type of flow.

2.3. *Validation*

Table 4 summarizes the results of the relevant studies previously discussed in the Introduction. It should be noted that the domain size and boundary conditions are not consistent from study to study. The experimental study of Bearman (1967) featured a blockage ratio of 3 % (with no blockage correction applied), whilst the studies of Pastoor *et al.* (2008) and Krajnovic & Fernandes (2011) featured 13 % blockage, as was the case here (no blockage correction was applied in the Krajnovic study). The non-dimensional numbers in this paper (Re_H, St, C_D, C_L, C_P and C_μ) were calculated using the corrected free-stream velocity $U_\infty = U\sqrt{B_c}$, where U is the inlet velocity

Study (year)	Method	Re_H	$C_{D,0}$	$C_{P,0}$	St	B_c	θ
Bearman (1967)	Exp.	41 000	—	−0.57	0.24	1.03	0.017
Park *et al.* (2006)	Exp.	40 000	—	−0.55	0.25	—	0.017
Pastoor *et al.* (2008)	Exp.	23 000	0.89	−0.53	0.23	1.32	0.017
Krajnovic & Fernandes (2011)[a]	Num.	23 000	0.77	—	0.27	1.32	—
Current study[b]	Num.	23 000	0.72	−0.53	0.22	1.27	0.019

TABLE 4. Comparison of natural flow results over a D-shaped bluff body. Entries above the horizontal line are included as an extra point of comparison, but feature slightly different geometries and experimental setups. [a] blockage correction has been applied by the present author, [b] mounts and no-slip domain walls not modelled.

and B_c is the blockage correction factor applied. Due to weak leading-edge separation, B_c was calculated using the general approach for bluff bodies in closed test section wind tunnels described by Hackett, Wilsden & Lilley (1979), as opposed to other techniques (such as that described by Mercker 1986), which are designed for cases with no leading-edge separation.

Furthermore, this study employs free-slip domain walls to remove the effect of sidewall boundary layers, compared with no-slip walls used in the studies of Pastoor *et al.* (2008) and Krajnovic & Fernandes (2011). This choice was dictated by the desire to reduce contamination of the wake from wall-junction flow structures, which, in turn, substantially influence mean lift and drag, so that the predictions here are more applicable to the infinite 2D cylinder case. Thus global measures, such as the mean drag (per unit width), may not be directly applicable between studies, but predictions for the centre plane, i.e. the base pressure coefficient ($C_{P,0}$) and the Strouhal number, provide a more relevant comparison. Here the agreement with the experimental results of Pastoor *et al.* (2008) for both the base pressure coefficient and Strouhal number is very good (within 5 % for both parameters).

The spanwise averaged wake velocity profiles for both natural (figure 4) and actuated (figure 5) cases show good agreement with Henning *et al.* (2007) and Krajnovic & Fernandes (2011). However, for both natural and actuated cases, the horizontal velocity profile shows a slightly lower velocity outside the wake than observed in the previous studies. This is most likely due to the top and bottom free-slip boundaries employed here, as simulations run at lower mesh resolutions with no-slip boundaries, matching the setup of the two previous studies, showed a similar increase in the flow speed as the outer flow approached the body. For the actuation case the peak vertical velocity at the edge of the wake is under-predicted, by both this study and Krajnovic & Fernandes (2011). The vertical velocity in the wake, however, agrees extremely well with the experiments.

The boundary layer momentum thickness θ at $X/H = -0.01$ compares well with previous experimental results. Even so, the effect of the boundary layer has not been analysed in great detail in the previous works. Pastoor *et al.* (2008) indicated that leading-edge separation occurred at $Re_H = 23\,000$, but not at higher Reynolds numbers. That the actuation remained effective despite this change in the flow over the leading edge suggests that the boundary layer characteristics have little impact on the drag reduction mechanism.

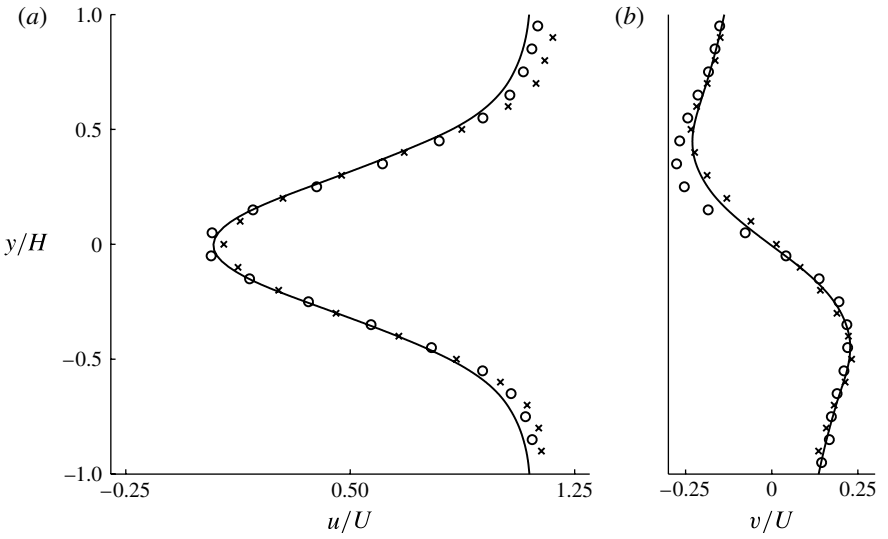

FIGURE 4. Unforced flow velocity profiles: comparison of the present study (solid line), Krajnovic's LES (2011) (circles) and Henning's PIV (2007) (crosses) at $X = H$ downstream of the rear face: (*a*) horizontal velocity and (*b*) vertical velocity. The prediction accuracy at other downstream locations is similar.

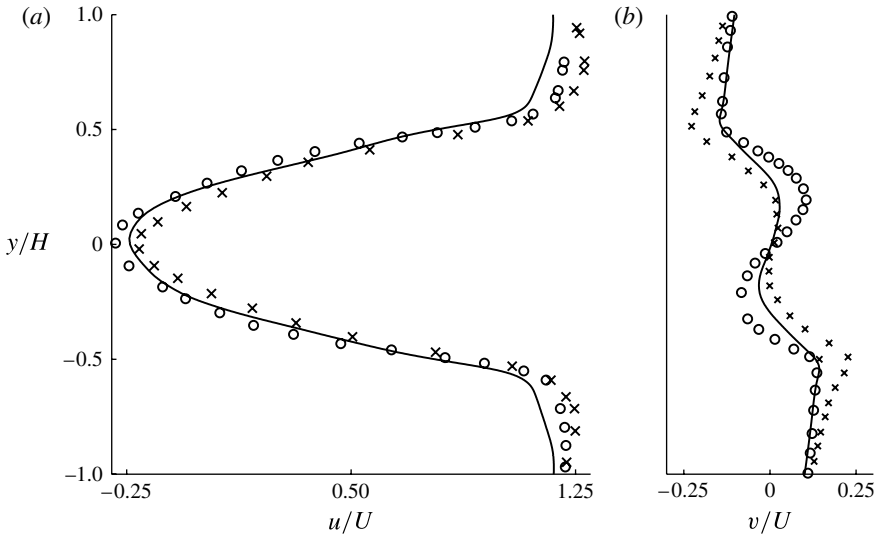

FIGURE 5. Actuated flow velocity profiles: comparison of the present study (solid line), Krajnovic's LES (2011) (circles) and Henning's PIV (2007) (crosses) at $X = 0.5H$ downstream of the rear face: (*a*) horizontal velocity and (*b*) vertical velocity. The prediction accuracy at other downstream locations is similar.

3. Results and discussion

3.1. *Natural flow: lift and drag*

The natural flow is characterized by weak separation over the leading edge with predominately spanwise aligned coherent flow structures forming as the flow convects

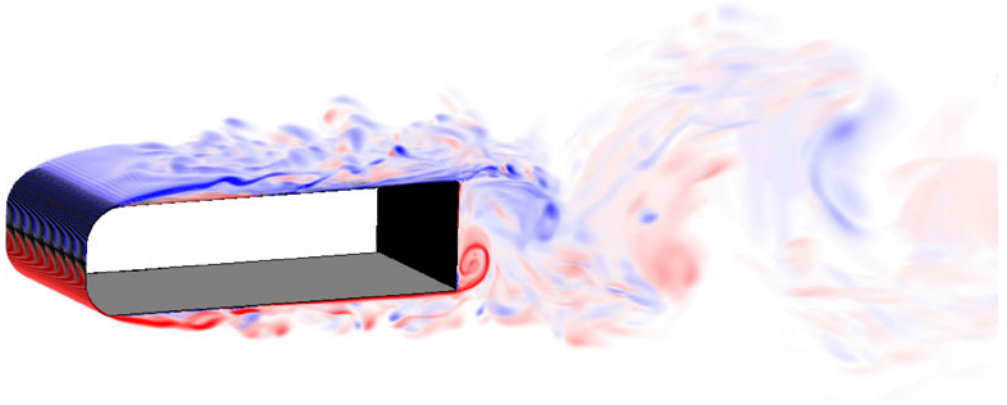

FIGURE 6. (Colour online) A snapshot of a perspective view of the instantaneous absolute spanwise vorticity for the natural flow over the body at $Re_H = 23\,000$. The flow is characterized by separation at the leading edges to form turbulent boundary layers, which separate at the rear edges to form a von Kármán wake further downstream. The red–white–blue colour map depicts spanwise vorticity from high to low levels (in black and white the darker regions indicate areas of greater spanwise vorticity magnitude).

towards the trailing edge, as shown in figure 6. An absolute instability in the wake (Huerre & Monkewitz 1990) results in large-scale von Kármán shedding from the rear separation points. While this shedding is 2D, the wake shows considerable 3D motion at smaller scales. The lift and drag coefficient history are shown in figure 7 together with power spectra for both signals at the right-hand side of the figure. Analysis using many periods of shedding are required before strong spectral peaks can be observed in the lift and, especially, the drag power spectra. The dominant lift frequency varies between $St = 0.22{\sim}0.23$, depending on the window used. A second peak occurs at $St = 0.15$. While a secondary peak at a similar frequency has been observed in 3D blunt trailing-edge flows (summarized in Grandemange, Gohlke & Cadot 2013), this has not been reported in the previous 2D studies. However, there also appears to be a low-frequency instability in the flow, which, although difficult to pick up with spectral analysis, can be seen in the alternating periods of lower and higher fluctuations in the lift and drag signals. It appears that this is related to the circular cylinder findings of Lehmkuhl *et al.* (2000), who attribute a low-frequency instability to shrinkage and enlargement of the recirculation zone. This can be seen as two different modes of wake configuration: a high-energy mode with larger shear-layer fluctuations and shorter recirculation region, and a low-energy mode with smaller fluctuations and longer recirculation zone. Here we observe an average recirculation zone of $1.1H$ in the low-energy mode (for example, between $t \equiv 70$–90 in figure 7) and $0.8H$ in the high-energy mode (between $t \equiv 90$–110.) This mechanism has yet to be explained.

Windowing was used to arrive at a final natural Strouhal number. The drag and lift signals were split into multiple windows of 30 non-dimensional time units, with fast Fourier transforms applied over each. For the majority of sample windows the dominant spectral peak occurs at $St = 0.44$ for the drag signal and $St = 0.22$ for the lift signal. (The drag peak frequency is double the lift peak frequency because each drag signal period represents one shed vortex, while each lift signal period represents two). While occasional periods of slightly higher shedding frequency are observed, we conclude that the predicted natural Strouhal number is 0.22, in good agreement with the experimental value obtained by Pastoor *et al.* (2008) of 0.23.

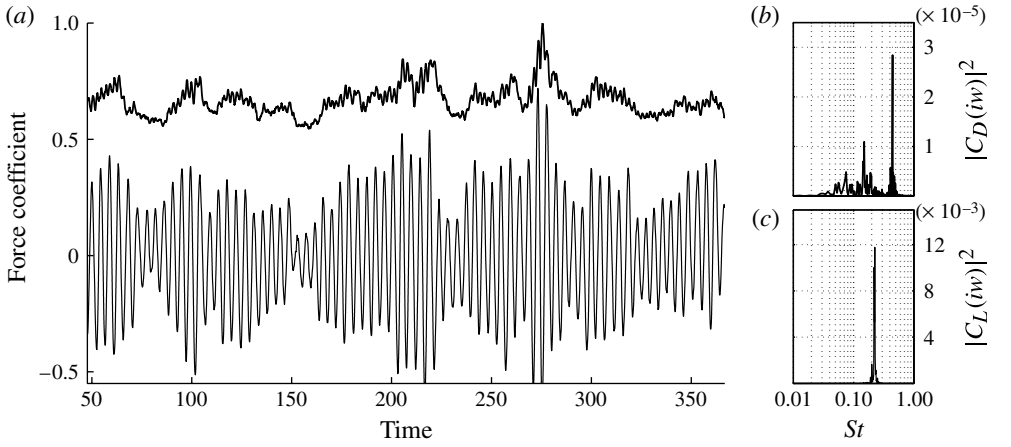

FIGURE 7. (*a*) Time history of drag (thick line) and lift (thin line) signals for natural flow, and (*b*,*c*) the frequency spectrum for each signal. The drag spectra amplitude (*b*) is displayed at a scale two orders of magnitude lower than the lift spectra amplitude (*c*). The lift signal returns a much clearer peak at the natural frequency than the drag signal.

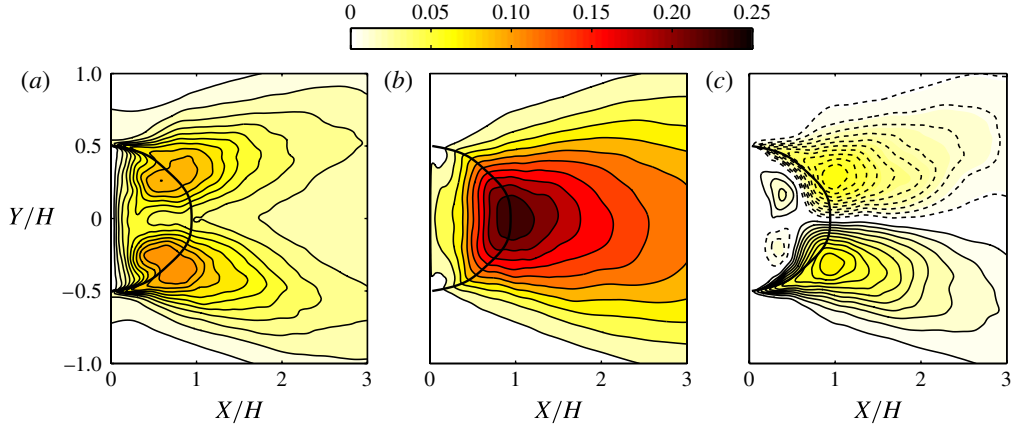

FIGURE 8. (Colour online) Reynolds stress averages along the centreplane in the wake: (*a* $\langle u'u' \rangle / U_c^2$, (*b*) $\langle v'v' \rangle / U_c^2$, (*c*) $\langle u'v' \rangle / U_c^2$. Dashed contour lines indicate negative magnitudes. The thick line indicates the separatrix (mean separation line).

3.2. *Natural flow: wake structures*

The normal Reynolds stress components are shown in figure 8. The normal cross-flow stress $\langle v'v' \rangle$ is by far the highest component in this case, peaking in the centre wake around $X/H = 1$ behind the rear face at the edge of the recirculation regions. The peak streamwise normal fluctuations $\langle u'u' \rangle$ occur in the centre of the recirculation region at approximately $X/H = 0.5$. The spanwise fluctuations $\langle w'w' \rangle$, by comparison, are less substantial. The shear stresses involving w' are also negligible.

The shear-stress $\langle u'v' \rangle$ plot reveals two distinct zones – one inside the recirculation region and one outside. The Reynolds stresses in the wake contribute to the

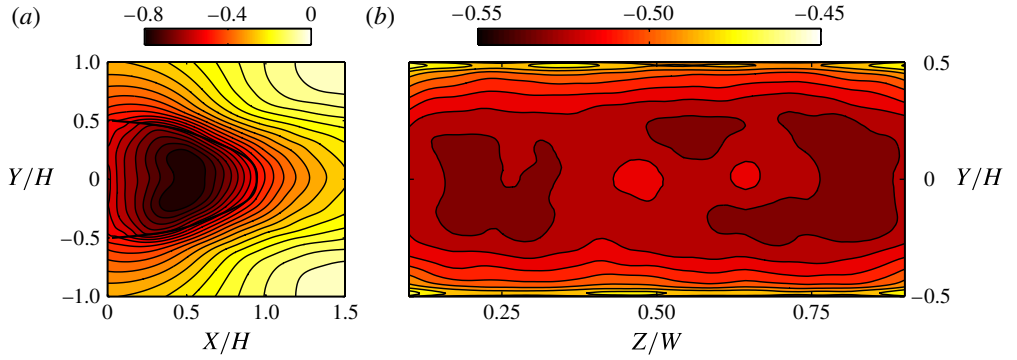

FIGURE 9. (Colour online) (*a*) Time-averaged pressure coefficient along the centreplane in the wake, and (*b*) on the rear base surface over $0.1 < Z/W < 0.9$. The thick line represents the separatrix.

equilibrium of the recirculation region – thus, where $\langle u'v' \rangle$ is zero approximates the mean recirculation boundary.

The time-averaged rear base pressure profile, which can be thought of as an 'output' parameter of the wake activity and directly responsible for drag, is shown in figure 9(*b*) (the outer edges $0 < X/H < 0.1$ and $0.9 < X/H < 1$, where mild end effects occur, are not shown). The pressure is shown to be slightly higher at the upper and lower edges, and relatively uniform over $-0.3 < Y/H < 0.3$. This pressure profile is dependent on the wake pressure profile (figure 9*a*). The minimum pressure occurs at the centre of each recirculation region – slightly above and below the centreline $Y/H = 0$, at $X/H \approx 0.5$). It is clear that, by increasing this minimum wake pressure and/or pushing its location further downstream, the rear base pressure will increase.

To analyse the wake further in terms of the dominant wake flow structures, a dynamic mode decomposition (DMD) was performed on the 2D velocity flow fields obtained at regular time intervals from the midplane of the wake. Dynamic mode decomposition was introduced by Rowley *et al.* (2009) and Schmid (2010), with further applications for fluid dynamics outlined in Schmid (2011) and Mezic (2013). The theoretical basis of this method is detailed in those papers, so only a brief outline of some important points will be given here. The process involves decomposing the flow into time-varying periodic spatial modes. The technique works on the assumption that each progressive flow field snapshot $\boldsymbol{x}_k$ is related by a matrix $\boldsymbol{K}$, a finite-dimensional approximation of the Koopman operator, such that $\boldsymbol{x}_{k+1} = \boldsymbol{K}\boldsymbol{x}_k$. The eigenvalues and eigenvectors of $\boldsymbol{K}$ represent the modes in the flow, and are separated by the motion frequency of each structure, as opposed to proper orthogonal decomposition (POD), which separates the modes from spatial information. Perhaps most importantly, for periodic data, the analysis is equivalent to a spectral decomposition, and presumably effectively close to spectral decomposition when the data are not strictly periodic. However, for growing or decaying instabilities, it can potentially isolate and localize the instability modes. Thus, the analysis produces a set of modes, each with its own growth rate and frequency. If the time sequence analysed has reached a statistically steady state, which is assumed here, then the growth rates of the modes should approach zero. The analysis also provides the amplitudes of each of the modes contributing to the original data set, thus allowing a low-order reconstruction of the data. In practice, care must be taken with the time-increment

between samples together with the total sampling time, just as is the case for standard spectral analysis of a time series. From a practical point of view, perhaps the most important result is that the m system snapshots (e.g. the set of velocity fields at times t_k), $\boldsymbol{x}_k$, can be reconstructed from the complex eigenvalues, λ_i, and complex eigenvectors or modes, $\boldsymbol{v}_i$ (commonly called Ritz values and vectors, respectively), by

$$[\boldsymbol{x}_0 \quad \boldsymbol{x}_1 \quad \cdots \quad \boldsymbol{x}_{m-1}] = [\boldsymbol{v}_1 \quad \boldsymbol{v}_2 \quad \cdots \quad \boldsymbol{v}_m] \begin{bmatrix} 1 & \lambda_1 & \lambda_1^2 & \cdots & \lambda_1^{m-1} \\ 1 & \lambda_2 & \lambda_2^2 & \cdots & \lambda_2^{m-1} \\ \vdots & & \vdots & \ddots & \\ 1 & \lambda_m & \lambda_m^2 & \cdots & \lambda_m^{m-1} \end{bmatrix}. \tag{3.1}$$

Thus the contribution from each DMD mode $\boldsymbol{v}_j$ to the snapshot $\boldsymbol{x}_k$ at time t_k is obtained by multiplying the mode by λ_j^{k-1}, with the amplitude of λ_j^{k-1} giving the amplitude multiplier, and the phase specifying the oscillation frequency. More details are given in Rowley *et al.* (2009). In general, the procedure used here follows the method described in Schmid (2010), and more information can be found therein.

DMD was applied to the natural flow spanwise averaged velocity fields over $0 < X/H < 4$ and $-1 < Y/H < 1$ (divided into a grid with 20 000 measurement locations and $\Delta x = \Delta y = 0.02H$), with the number of samples $m = 117$, which covers a period of nine complete vortex shedding cycles. The time between each sample was $\Delta t_s = 0.005$ s, equating to approximately 13 samples per shedding period. It was confirmed that these numbers obtained effectively a complete vector space (higher m values produced near-identical results). The results, shown in figure 10, indicate that the wake is dominated by only one dynamic mode, together with the mean mode. Not surprisingly, the frequency of this mode corresponds to the observed (uncorrected) shedding frequency of $St = 0.23$. Notably the spectrum at the top right shows that the first harmonic of that mode is also discernible. Even so, its relative low amplitude indicates that the wake flow associated with the dominant mode (N) together with its harmonics is not too far from sinusoidal.

Figure 11 shows the vorticity evolution over a cycle for the dominant time-dependent Koopman mode (N). This mode shows that a pair of co-rotating vorticity perturbations forms from each trailing edge of the body, with each new pair having the opposite direction of rotation to the previous pair. These two vortices quickly come together to form one large vortex, which proceeds downstream. While the co-rotating nature of the vortices in this mode may seem unexpected, it should be recalled that this mode exists superimposed on the mean mode (M), which features two counter-rotating regions of vorticity, as shown in figure 10(c), and does not change with time. Thus, when the first dynamic mode N and mean mode are added together in figure 12, it can be seen that one of the mode N co-rotating vortices is amplified by the similarly signed vorticity region in the mean mode, whilst the other is nullified by the opposite-signed vorticity region. We therefore end up with traditional von Kármán shedding: asymmetric vortex shedding resulting in a von Kármán vortex street progressing downstream. This accounts for the dominant time-dependent features of the unsteady wake, as can be seen from a comparison with the phase-averaged evolution shown in figure 13.

3.3. *Periodic actuation*

Periodic actuation was applied from the rear slots after the natural flow had settled into a consistent transient response pattern (∼140 non-dimensional time units). The

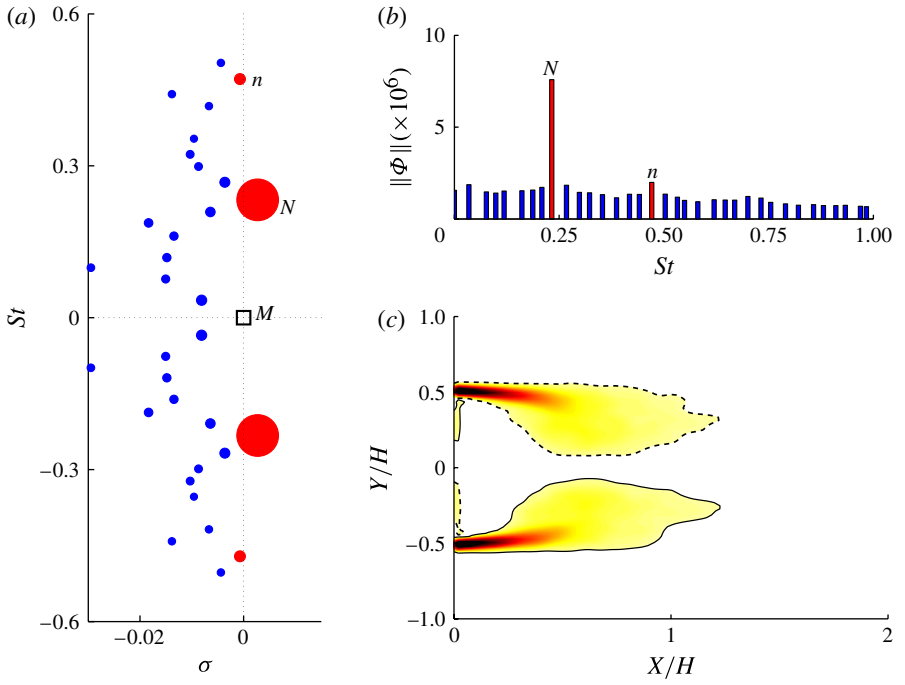

FIGURE 10. (Colour online) Natural flow dynamic mode decomposition. (*a*) Spectrum showing the growth rate (σ) of each mode. The red dots are the most relevant modes, with the size of each dot showing its relative magnitude. The mean mode (M) is indicated with an open square. Mode N occurs at the natural Strouhal number and mode n at the first harmonic of N. (*b*) Relative magnitude of each mode plotted against frequency. (*c*) Vorticity contours for the mean mode.

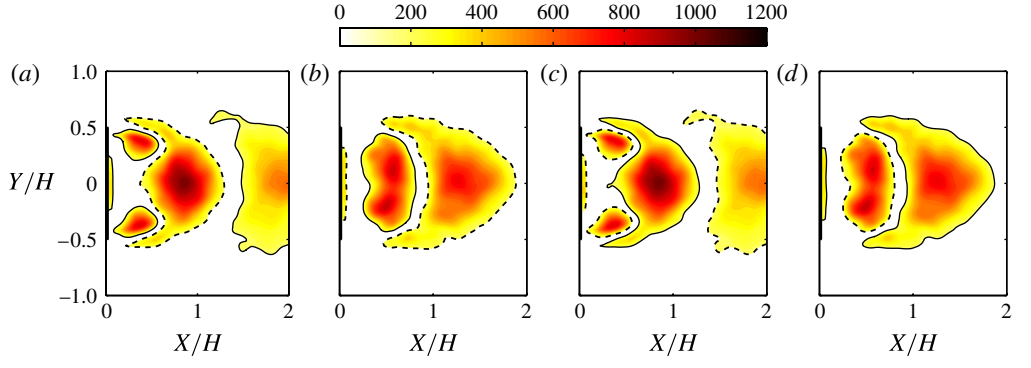

FIGURE 11. (Colour online) Natural flow: vorticity contours of one complete cycle of the first Koopman mode (also referred to as the natural mode), i.e. mode N. Dashed line, clockwise vorticity; solid line, anticlockwise vorticity. The sequence progresses left to right, with each image progressing one quarter step through the cycle from the previous image.

progression of the drag and lift coefficients for $St_{act} = 0.11$ can be seen in figure 14. As found for all actuated cases, settling time is relatively short (∼10 time units or less), with the actuation regulating the drag signal almost instantly. However,

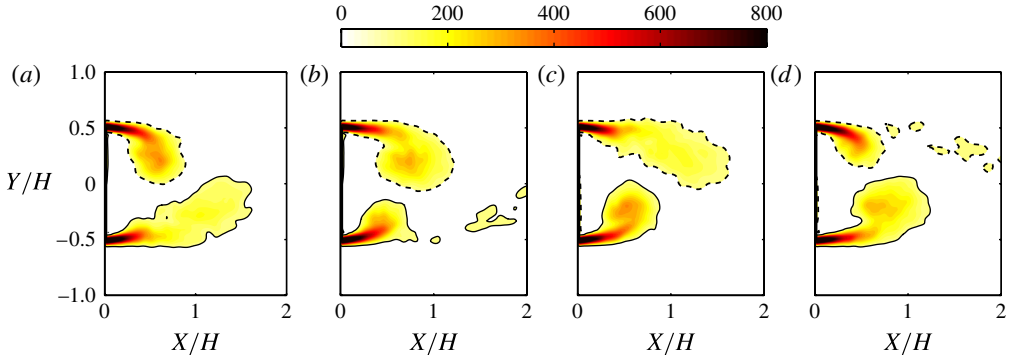

FIGURE 12. (Colour online) Natural flow: reconstruction of the vorticity evolution for the natural flow using just the Koopman mean mode M and the larger-amplitude DMD mode N.

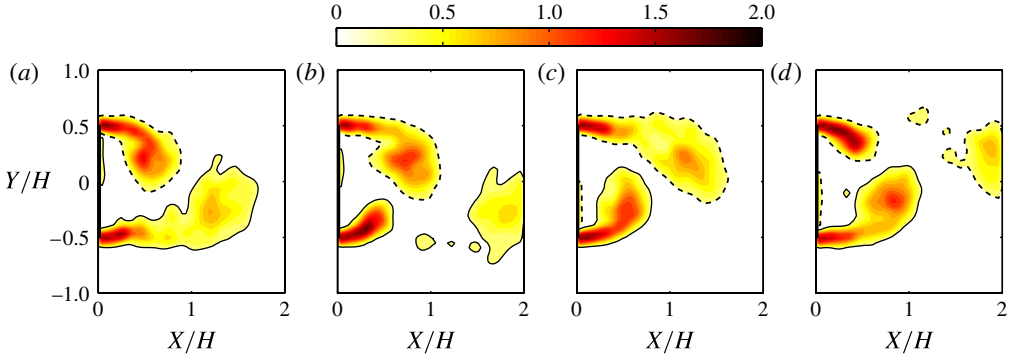

FIGURE 13. (Colour online) Natural flow: vorticity contours of one complete cycle of the phase-averaged observed flow field. A similar wake evolution is observed to that of the Koopman reconstruction using only modes M and N (figure 12).

figure 15 reveals that the fidelity of the signal differs from case to case. The lowest frequency $St_{act} = 0.04$ drag signal, for example, notably features small perturbations superimposed on the larger-amplitude wave (figure 15*a*). Spectral analysis of this case reveals a weak secondary frequency peak at the Strouhal frequency, indicating that two modes may be coexisting in the wake. The next-lowest frequency cases shown, $St_{act} = 0.09$ and $St_{act} = 0.11$, also display some semblance of this behaviour. As the actuation frequency is increased, the corresponding drag signal appears to become more periodic.

The lift signal (also displayed in figure 15) also differs from case to case. Perfectly symmetrical shedding would theoretically result in a contribution of zero lift from the wake. It might be expected that the measured r.m.s. lift value follows a similar trend to the mean drag value, and that is precisely the case. At $St_{act} = 0.04$ the signal alternates in a manner similar to the natural case, with a large peak in a spectral analysis occurring at $St = 0.23$. As the actuation frequency increases, however, the periodicity of the lift signal appears to break down, before returning when the actuation is close

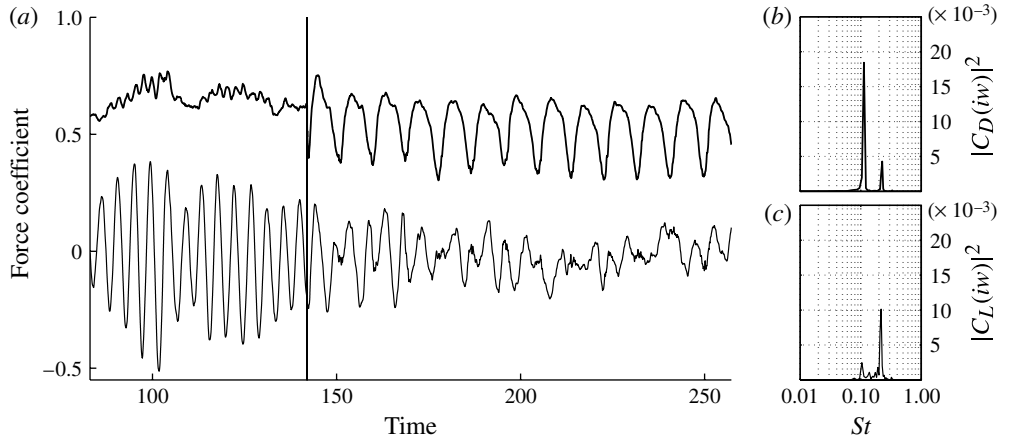

FIGURE 14. (*a*) Time history of drag (solid line) and lift (dashed line) signals for $St_{act} = 0.11$, and (*b*,*c*) the frequency spectrum for each signal. The drag spectra amplitude (*b*) is displayed at the same scale as the lift spectra amplitude (*c*). The drag signal returns a much clearer peak than the lift signal. The discontinuity at $t = 140$ corresponds to the switch from unforced to forced flow.

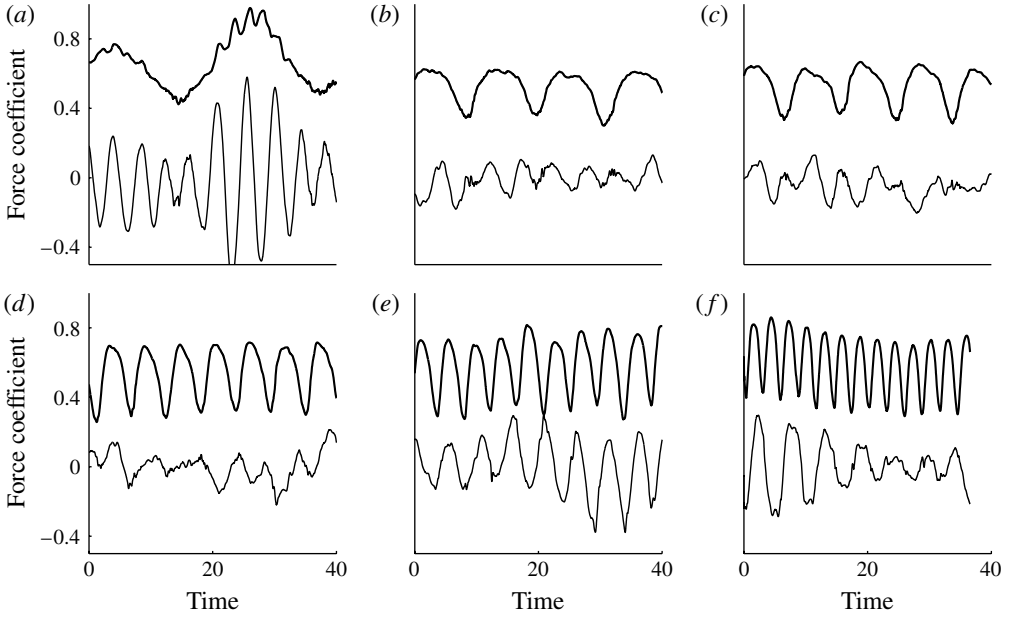

FIGURE 15. Sample of drag coefficient (higher, thick line) and lift coefficient (lower, thin line) signals for various actuation signals: (*a*) $St_{act} = 0.04$, (*b*) $St_{act} = 0.09$, (*c*) $St_{act} = 0.11$, (*d*) $St_{act} = 0.18$, (*e*) $St_{act} = 0.23$, (*f*) $St_{act} = 0.35$.

to the natural Strouhal frequency at $St_{act} = 0.23$. At yet higher frequencies, the signal becomes less periodic again, but not as much as observed at the lower actuation frequencies.

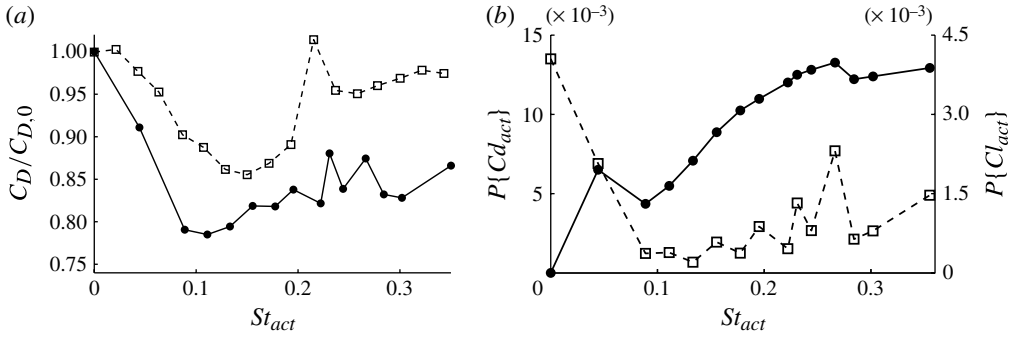

FIGURE 16. (*a*) LES results (solid circles) for mean drag at different actuation frequencies. Minimum drag is obtained at $St_{act} = 0.11$. Experimental results from Pastoor *et al.* (2008) (actuation applied over only half of the span) are also shown (open squares). (*b*) Amplitude of actuation frequency spectral peaks ($P\{Cd_{act}\}$) for the drag signal (solid circles) and Strouhal frequency spectral peaks ($P\{Cl_{nat}\}$) for the lift signal (open squares).

The power spectra recovered from fast Fourier transforms of the drag and lift signals (figure 16*b*) quantify this behaviour. The peak response in the drag spectrum always occurs at the actuation frequency (we denote this by $P\{Cd_{act}\}$), while the peak in the lift spectrum always occurs very close to the natural Strouhal frequency (this is denoted $P\{Cl_{nat}\}$). As the actuation frequency increases, so does $P\{Cd_{act}\}$, peaking at $St_{act} = 0.23$. This is consistent with Pastoor *et al.* (2008). However, it appears that this value is not the crucial factor in determining optimal drag reduction: $P\{Cl_{nat}\}$ closely mirrors the drag reduction (again, also observed by the Pastoor group), and it appears that minimizing this value is the key. Indeed, $P\{Cl_{nat}\}$ also correlates strongly with the aforementioned r.m.s. lift signal value, which is indicative of asymmetry in the wake. These lift measurements make it clear that optimal drag reduction corresponds with reduced asymmetry in the wake.

The final drag reduction results (figure 16*a*) show there is an optimal actuation frequency range between $St_{act} = 0.09$ and $St_{act} = 0.135$, with the effect slowly decreasing as actuation frequency increases. A maximal drag reduction of 20 % occurs at $St_{act} = 0.11$. By comparison, Pastoor *et al.* (2008) found an optimum reduction of 16 % at $St_{act} = 0.15$. Again, recall that in the experiments the 7:1 aspect-ratio body extended across the entire working section of the tunnel, and hence end effects would not be negligible. In addition, it was only actuated over half the span, thus some difference in the optimal actuation Strouhal number between the simulations and experiments might be expected. A noticeable peak is seen at $St_{act} = 0.23$, where the actuation frequency corresponds to the natural Strouhal frequency. This peak, not as large as that observed by the Pastoor group, coincides with a moderate strengthening of the natural wake instability, which does not occur for the other cases. At $St_{act} = 0.265$ another peak is observed, which is discussed in the DMD analysis below.

Analysis of the time-averaged wake reveals that the separatrix (marking the mean recirculation bubble) for the optimum case ($St = 0.11$) is noticeably longer than for the unforced case, as shown in figure 17. This longer formation length is due to the suppression of the von Kármán shedding caused by the rear-edge actuation: strong shear-layer perturbation prevents the immediate development of an asymmetric wake. Larger-scale upper and lower shear vortices eventually do develop (the vortex roll-

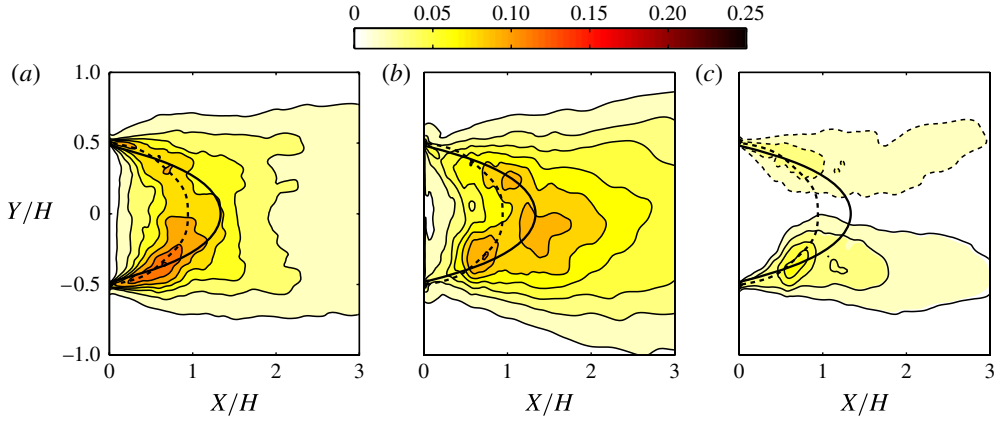

FIGURE 17. (Colour online) Reynolds stress averages along the centreplane in the wake: (*a*) $\langle u'u' \rangle / U_c^2$, (*b*) $\langle v'v' \rangle / U_c^2$, (*c*) $\langle u'v' \rangle / U_c^2$. Dashed contour lines indicate negative magnitudes. The thick line indicates the separatrix (mean separation line); the dashed thick line indicates the separatrix of the unforced case.

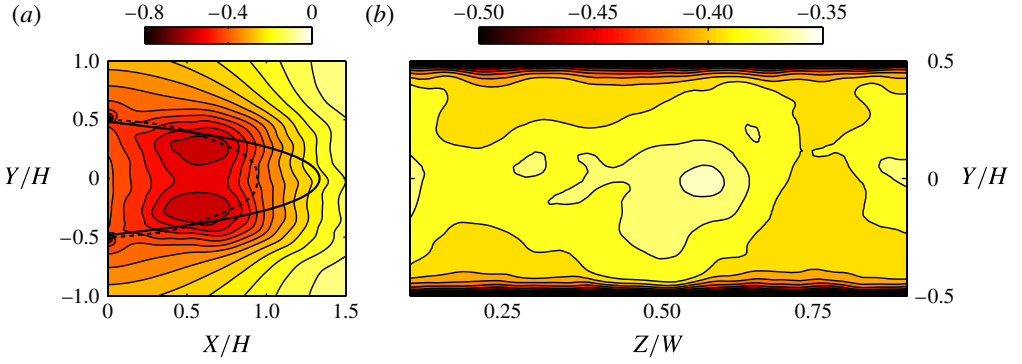

FIGURE 18. (Colour online) Time-averaged pressure coefficient along the centreplane in the wake (*a*) and on the rear base surface over $0.1 < Z/W < 0.9$ (*b*). The thick line represents the separatrix.

up is initiated by the induced velocity of the previously shed vortex pair) and are shed synchronously. Asymmetry eventually returns further downstream. The Reynolds stress contours, also shown in figure 17, reveal a strong reduction in the normal cross-flow stress $\langle v'v' \rangle$. Furthermore, the shear stress $\langle u'v' \rangle$ is much reduced in the near wake. The time-averaged wake pressure is considerably higher than for the natural case. Of further note is the distribution of this pressure: for the natural case the pressure varies greatly with respect to Y, with a minimum occurring at $Y = 0$, whereas in the actuated case the pressure is relatively uniform over the range $-0.5 < Y/H < 0.5$. This translates to a rear base pressure profile which is uniformly higher over $-0.45 < Y/H < 0.45$. By comparison, the natural case was uniform only over the narrow range $-0.3 < Y/H < 0.3$.

While these time-averaged results certainly have a use in developing an understanding of the flow, they do not reveal the full details of the dynamic

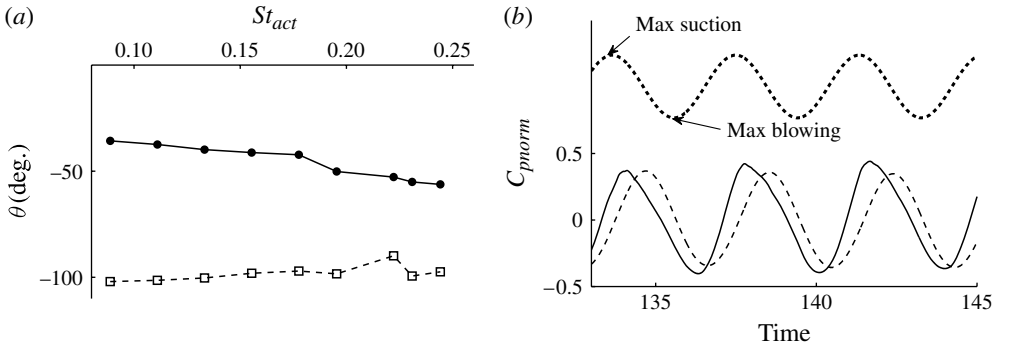

FIGURE 19. (*a*) The lag in phase between the actuation signal and the rear base pressure (solid line) and stagnation pressure (dashed line) as the actuation frequency is varied. (*b*) A comparison of the actuation signal time history (dotted line) with the normalized rear base pressure $C_{bp} - \overline{C_{bp}}$ (solid line) and stagnation pressure response (dashed line) for $St_{act} = 0.23$.

mechanisms operating in the wake. The following discussion first analyses the relationship between various signals in the flow, before exploring both the observed transient wake measurements and lower-order representations.

The stagnation pressure at the front of the body interestingly shows a strong correlation with the actuation signal. Separation occurs over the leading edge, creating leading-edge vortices that travel downstream before interaction with the trailing-edge vortices. Previous work by Rockwell & Naudascher (1979), Hourigan, Thompson & Tan (2001) and Mills, Sheridan & Hourigan (2001) (amongst others) has shown that the trailing-edge vortex formations can have a profound feedback effect on the leading-edge vortices. In fact, Mills *et al.* (2001) showed that the rate of leading- and trailing-edge vortex shedding become locked in together for certain conditions. Here we see a similar effect: the stagnation pressure oscillates significantly at a moderate delay from the rear base pressure, which in turn is slightly delayed from the actuation signal. The small wind tunnel size used by Pastoor *et al.* (2008), and replicated in virtual space here, was found to be amplifying this effect: simulations run at a larger domain size showed a significant drop in the amplitude of the stagnation pressure fluctuation. It remains unclear how large the amplitude would be in an infinitely large domain, although the previously mentioned research by Mills *et al.* (2001) suggests that the feedback is expected on some level. This effect does not impact the mean stagnation pressure, meaning that its effect on the mean drag measured is negligible (it does, of course, increase the amplitude of the drag fluctuations recorded). Indeed, the drag reduction measured for $St_{act} = 0.135$ at the larger domain size was identical to that measured at the smaller domain size. The stagnation pressure phase difference appears to remain fairly constant for each case at close to a 100° delay. The rear base pressure measurement signal also locks on to the actuation signal for all cases, with a small lag in the phase between the actuation signal and the response gradually increasing with actuation frequency from 35 to 55°, as seen in figure 19(*a*).

Figure 19(*b*) shows that maximum drag (minimum base pressure) occurs at maximum blowing, while minimum drag occurs at maximum suction. The phase-averaged vorticity progression of a typical actuation cycle, shown in figure 20, elucidates this. The new shear-layer development begins just after the actuation switches from blowing to sucking (between figures 20*b* and 20*c*). Meanwhile, the

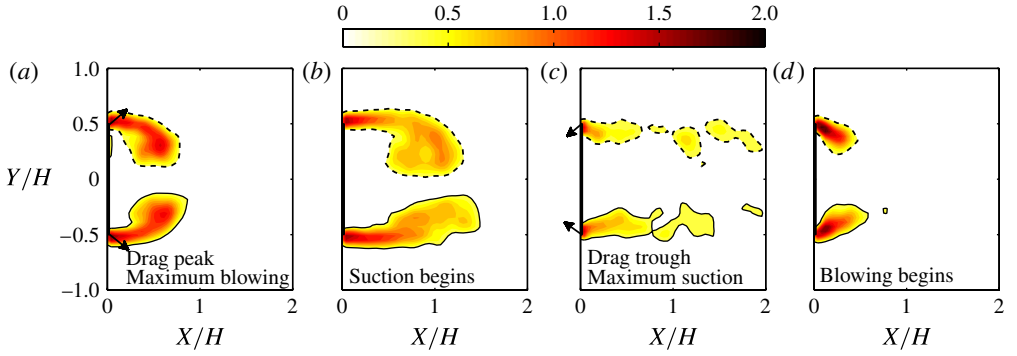

FIGURE 20. (Colour online) $St_{act} = 0.11$: vorticity contours of one complete cycle of the phase-averaged flow field. Dashed line, clockwise vorticity; solid line, anti-clockwise vorticity. (*a*) Drag signal peak, (*b*) halfway between drag signal peak and trough, (*c*) drag signal trough, (*d*) halfway between drag signal trough and peak. A rapid decrease in vorticity, presumably due to diffusion and cross-annihilation, is observed once the symmetrically shed vortices interact. Arrow directions are a simplified representation of the actuation at each snapshot (no arrows indicate that the actuation is halfway between blowing and sucking or vice versa). Flow is from left to right.

previous vortex pair have detached and begun to interact in the wake. By the time maximal suction has been reached (figure 20*c*), this cross-annihilation has left the wake with considerably reduced vorticity levels, and the new upper and lower shear layers, while still small, begin to be drawn into the wake and roll up into vortices. When actuation switches from sucking to blowing (figure 20*d*), these new vortices have reached a medium size, leading to a steady rise in drag and, once maximal blowing is reached (figure 20*a*), they have formed large coherent structures, which results in a peak in the drag signal. As the blowing reduces, they travel downstream, with drag decreasing once again, and the process repeats. The large amplitude of the drag signal is due to the combined effect of the vortices both developing together (high drag) and then convecting downstream together and destructively interacting with one another (low drag). When compared against the natural progression shown in figure 13, the effect of the actuation is apparent: the vortex shedding is symmetric, extending formation length and raising the pressure in the near wake and lowering drag.

Dynamic mode decomposition of the spanwise averaged velocity fields reveal the presence of a new mode in the flow due to actuation (mode A) that is not observed for the natural case. This mode appears to coexist with mode N of the natural case (the mean mode M is also effectively identical to that of the natural case). Vorticity contours of mode A (figure 22) show a symmetric structure about $Y = 0$, with two pairs of opposite-signed vortices created and shed per cycle (while the opposite-signed vortices at first glance appear to form an anti-symmetric structure, if we reflect the positive direction of vorticity across $Y = 0$, we can describe the mode as symmetric). Each vortex in this mode first develops on the inside of the shear layer, with the previous vortex of opposite sign still attached in the shear layer region. Once the previous vortex breaks from the shear layer, the new vortex then grows in this area. When mode A is superimposed on the non-dynamic mode M, each pair of mode A vortices alternately either amplifies the mean mode vorticity of each shear layer (creating a large pair of synchronous vortices), or nullifies it (leaving an 'empty'

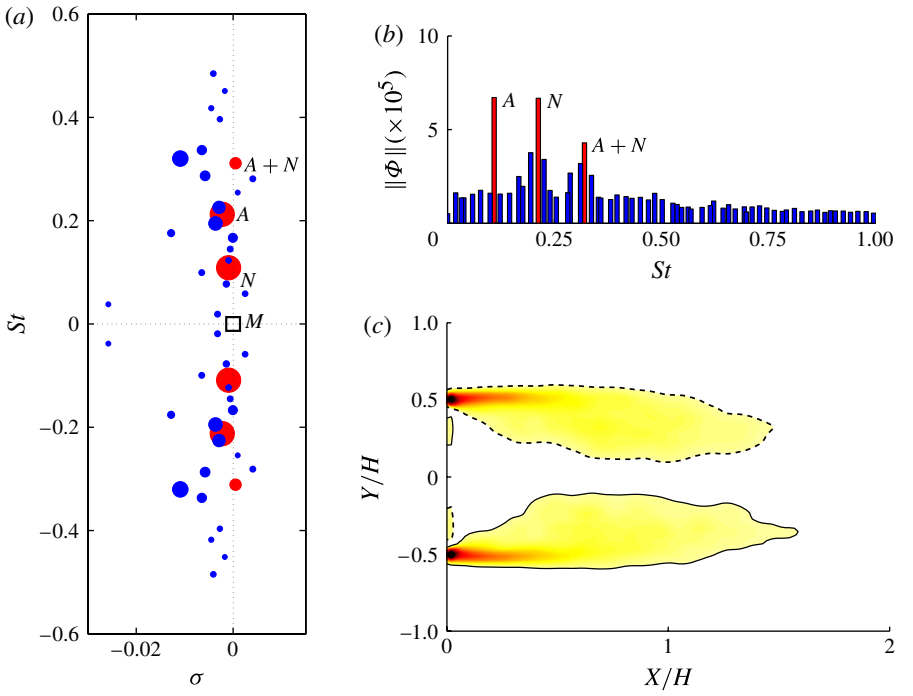

FIGURE 21. (Colour online) Dynamic mode decomposition for $St_{act} = 0.11$. (*a*) Spectrum showing the growth rate (σ) of each mode. The red dots are the most relevant modes, with the size of each dot showing its relative magnitude. The mean mode (M) is indicated with an open square. Mode N occurs at the natural Strouhal number and mode $A + N$ at the sum of frequencies N and A. (*b*) The relative magnitude of each mode is plotted against frequency. (*c*) Vorticity contours for the mean mode.

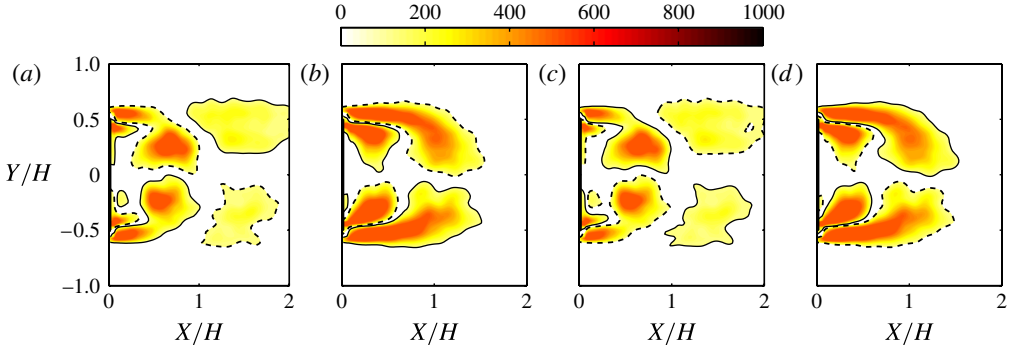

FIGURE 22. (Colour online) $St_{act} = 0.11$: vorticity contours of one complete cycle of the first unsteady Koopman mode (mode A).

wake), resulting in a significant change in near-wake pressure throughout the cycle. It appears that perfect symmetric shedding would be achievable if this were the only dynamic mode in the wake. However, as mentioned above, the symmetric mode N of the natural case is also present in the wake. For most cases this mode operates at a

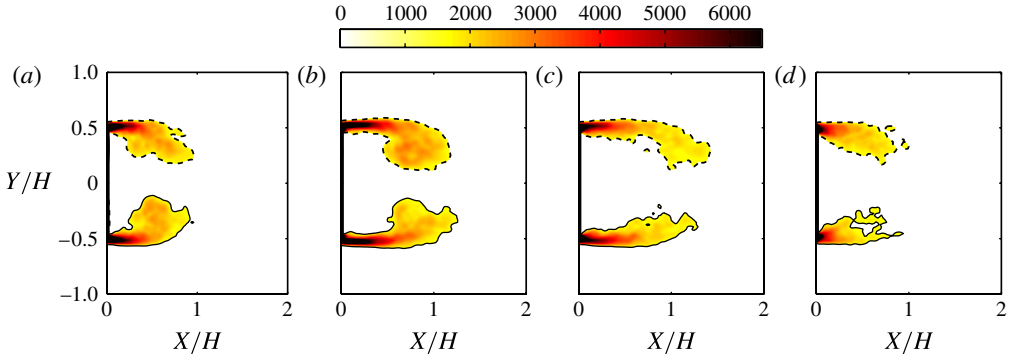

FIGURE 23. (Colour online) $St_{act} = 0.11$: reconstruction of the vorticity evolution over one complete cycle using the Koopman mean mode and the first two unsteady Koopman modes (modes A and N).

different frequency to mode A, and thus will impact the symmetric shedding process in different ways from case to case, and cycle to cycle. The interplay of these modes – the actuation and natural – appears to be a dominant mechanism in the flow. Indeed, for each case a reconstruction using only these modes recovers the majority of features seen in the observed phase-averaged flow; figures 20 and 23 show this for the optimal case of $St_{act} = 0.11$.

However, while the structure of mode A appears to vary little as the actuation frequency is varied, the same cannot be said of mode N. Over certain intervals the mode N structure appears close to the non-actuation case, while over others it loses coherency. Moreover, the frequency of the mode St_N fluctuates from case to case: it remains close to the natural value $St = 0.23$ for the low-frequency actuation cases but drops to $St = 0.195 \pm 0.015$ for all cases with $St_{act} \geqslant 0.135$. Despite this varying nature, measuring the magnitude of the mode $\Sigma|K_N|$ (the sum of the Koopman eigenvector magnitudes at each point in the wake) for each case does provide some insight, as shown in figure 24. In the higher frequency range, it appears that $\Sigma|K_N|$ shows a strong correlation with C_D; the two drag peaks $St_{act} = 0.23$ and $St_{act} = 0.265$ feature substantially higher mode N magnitudes. The natural mode seems to be more excitable in this regime, but the exact amplitudes may be due to the finite sampling time, However, it appears reasonable that this occurs with actuation near the original natural frequency, although it must be remembered that it is higher than St_N, the frequency of mode N. In the lower-frequency range, however, the correlation is somewhat less strong, with one of the optimal drag reduction cases, $St_{act} = 0.09$, still featuring a relatively high mode N magnitude.

The magnitude of mode A, also, does not appear to be an indicator of drag reduction success: it is seen to be highest both slightly above and below the mode N frequency $St_N \approx 0.195$, yet is relatively low for two of the optimal drag reduction cases $St_{act} = 0.09$ and $St_{act} = 0.11$. At $St_{act} = 0.195$ the magnitude of both modes A and N drops, suggesting that when the actuation frequency is close to the expected $St_N \approx 0.195$, the two modes are less successful at coexisting. Yet, even for this case, no significant change occurs in drag reduction. It is clear that there is more to achieving optimal drag reduction than simply creating a prevalent symmetric mode A and weakening mode N. But what other mechanism could be responsible?

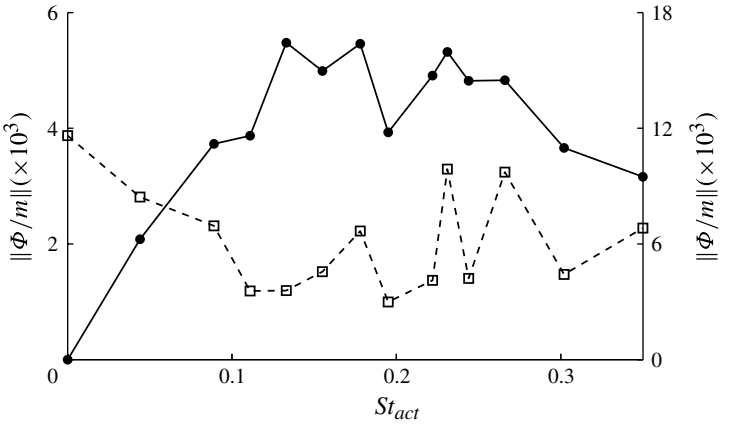

FIGURE 24. Magnitudes of Koopman modes A (left axis, solid dots, continuous line) and N (right axis, open squares, dashed line) for each actuation frequency St_{act}. Magnitudes are normalized by m, the total number of snapshots used in the DMD.

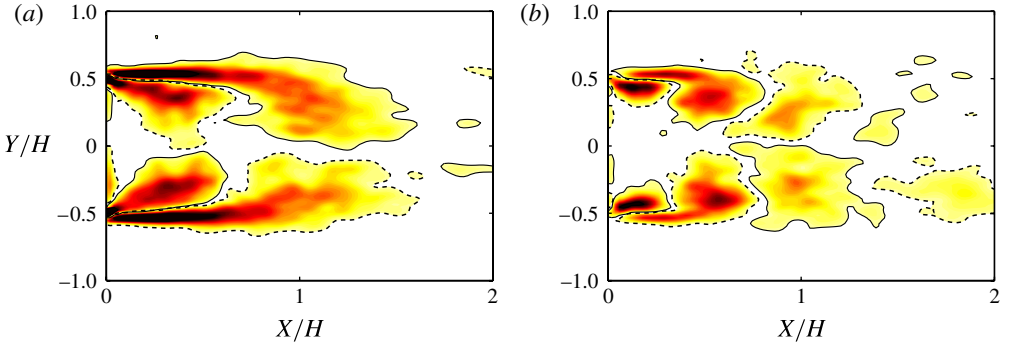

FIGURE 25. (Colour online) Vorticity contours of actuation mode for (*a*) $St_{act} = 0.11$ and (*b*) $St_{act} = 0.35$. The size of the mode A vortices is significantly less for the higher-frequency actuation case.

It appears that the answer lies in the changing characteristics of the mode A vortices at different actuation frequencies, and their superposition with mode N in the near wake. Figure 25, which shows a snapshot of mode A for a lower-frequency case ($St_{act} = 0.11$) and a higher-frequency case ($St_{act} = 0.35$), makes this difference clear: high-frequency actuation creates mode A vortices smaller than those created with low actuation frequencies. While both cases appear to generate vortices with a similar peak vorticity, the larger area of the lower-frequency vortices results in a greater total circulation per vortex, which, of course, is connected to the different times that the shear-layer vorticity feeds into the wake vortices. Furthermore, as shown in figure 26(*a*), the centres of the low-frequency vortices are observed to approach the wake centreline much more closely than the higher-frequency vortices. This proximity to the centreline, coupled with their larger area and circulation allow the low-frequency mode A vortices to diminish the impact of the coexisting mode N vortices which become prevalent on the centreline of the wake at $X/H \approx 0.6$ and further downstream.

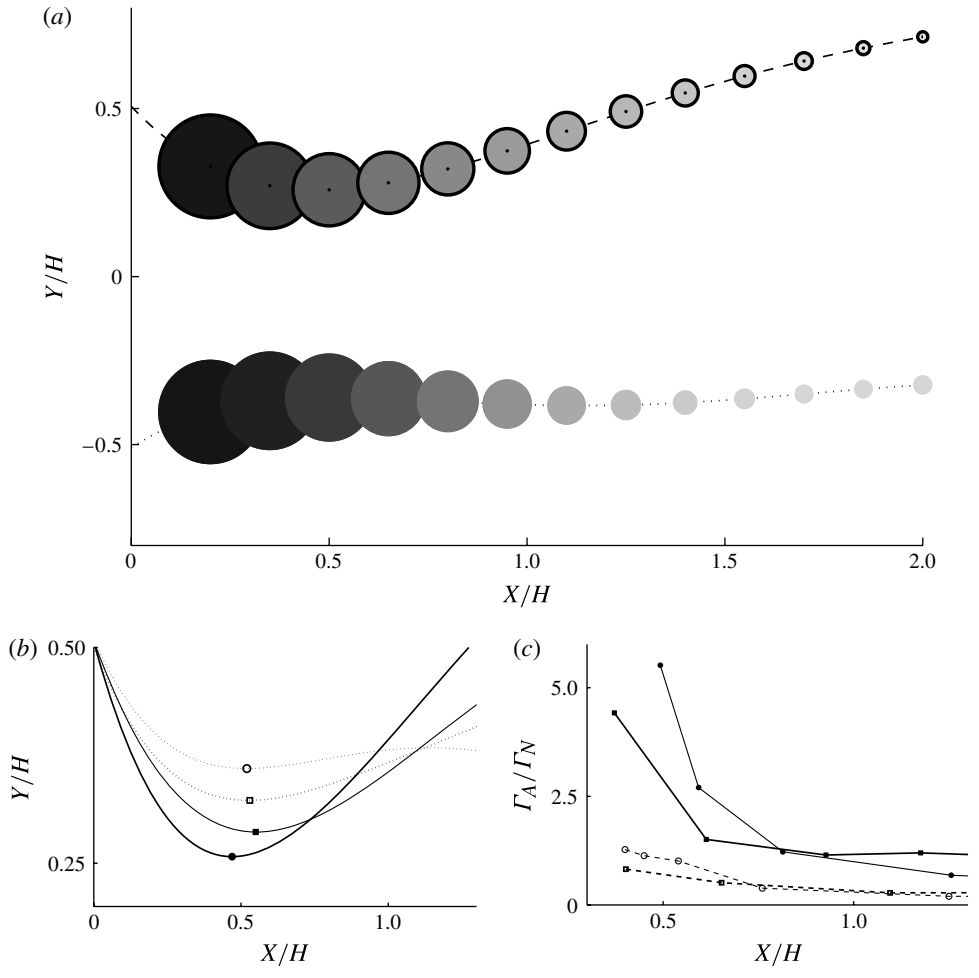

FIGURE 26. (*a*) Comparison of a typical mode *A* vortex path for cases $St_{act} = 0.09$ (upper circles with thick edges) and $St_{act} = 0.35$ (lower circles with no edges). The size and shading of each circle represents the average vorticity of the vortex (circulation per unit area). (*b*) The near-wake path of a typical mode *A* vortex for four cases for $St_{act} = 0.09$ (thick solid line), $St_{act} = 0.135$ (thin solid line), $St_{act} = 0.27$ (thick dashed line), and $St_{act} = 0.35$ (thin dashed line). (*c*) The ratio of mode *A* circulation to mode *N* circulation as a function of the downstream location. Line styles represent the same cases as in (*b*).

At higher frequencies, the smaller circulation of the mode *A* vortices and greater distance from the centreline weakens their influence on the final wake once the modes are superimposed. This was checked by calculating the vorticity of numerous mode *A* and *N* vortices for each case, and comparing the ratio Γ_A to Γ_N as a function of downstream location. The circulation values were obtained by using the Γ_2 approach outlined in Graftieaux, Michard & Grosjean (2001) to identify the vortex and finding the integral of the spanwise vorticity over the area enclosed by the identified contour. Figure 26(*c*) shows a significant drop in the influence of mode *N* in the near wake for the lower frequency cases. This results in a higher near-wake pressure and lower drag.

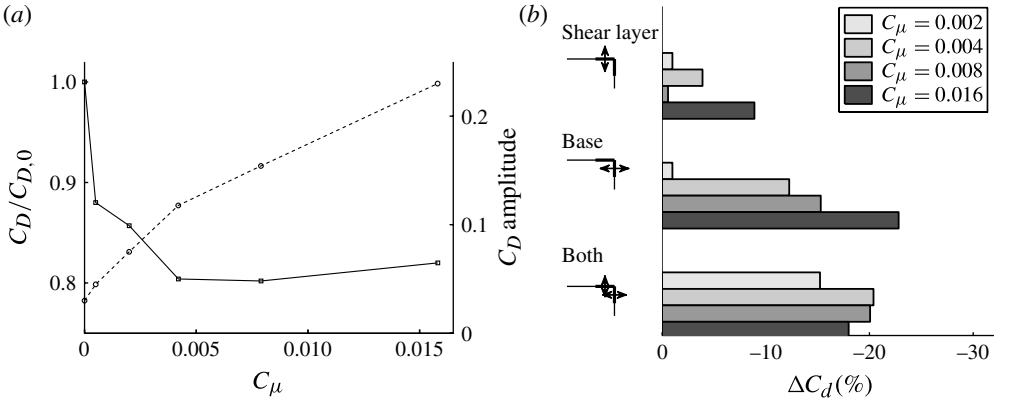

FIGURE 27. (*a*) Drag reduction (solid line) as a function of the actuation momentum coefficient for optimum frequency case ($St_{act} = 0.11$). The dashed line represents the mean amplitude of the drag coefficient signal. (*b*) Effect of actuation from different configurations at $St_{act} = 0.11$. μ is the total momentum coefficient (not the individual momentum coefficient of each actuator).

In summary, it has been shown that there are a number of factors behind the success of in-phase actuation at the rear edges of a bluff body. Creating successful synchronous shedding is not the only requirement to achieve optimal results: if the shedding is generated at a high frequency, the smaller vortices are not able to distort the natural mode *N* centreline vortices as effectively, resulting in lower drag reduction. Thus, lower frequencies are more effective, as long as they are not so low that the actuation-controlled shear-layer development is not able to dominate the natural instability. At too low a frequency (for example, at $St_{act} = 0.04$), however, the persistence of the natural flow fluctuations does not allow mode *A* to develop properly.

3.4. *Momentum coefficient and actuation orientation*

As a follow-up to this sub-study on the effect of actuation frequency, the influence of momentum coefficient was also explored. The results obtained for the optimum-frequency case of $St_{act} = 0.11$ (see figure 27*a*) show that significant drag reduction is possible at lower momentum coefficients, and no further reduction gains occur for $C_\mu \geqslant 0.004$ in spite of the continued growth of the drag coefficient amplitude (about the mean). In comparison, Pastoor *et al.* (2008) found a threshold value of 0.008. However, their actuation was applied over only half the spanwise width of the trailing edge – effectively halving the true momentum they were injecting to the flow. Thus the threshold value of 0.004 for these simulations appears consistent. They also found a minimum threshold value $C_\mu \simeq 0.005$ (which becomes 0.0025 if we correct it as above), below which minimal drag reduction is achieved. This is clearly at odds with the finding of these tests that reasonable drag reductions can be achieved with momentum coefficients below even 0.001. One possible explanation could be the difference in the fidelity of the applied actuation signals. In this numerical work the signal is naturally perfectly sinusoidal, even at lower amplitudes. It is well known, however, that low-amplitude noise makes achieving clear low-amplitude sinusoidal signals in actual experiments especially difficult, while high-amplitude signals are able to mask the noise. While this is beyond the scope of this paper, it seems plausible that signal fidelity may be an important consideration for practical actuation.

However, such success at lower momentum coefficients was not observed at a higher-frequency actuation case, $St_{act} = 0.30$, which showed a minimum threshold of $C_\mu \approx 0.003$. This suggests that each actuation frequency has its own minimum threshold value, which is likely to be lower for the most successful actuation frequencies.

In any case, actuation at $C_\mu \simeq 0.004$ seems the appropriate level for peak drag reduction at highest efficiency. In addition to other points discussed previously, this may add to the explanation as to why the optimal St_{act} of 0.11 is lower than that observed in the experiments by the Pastoor group (0.15). Just as clean lower-amplitude signals are more difficult to generate experimentally, so are lower-frequency signals. It could be possible that frequencies around $St \simeq 0.11$ are most effective if the actuated signal is clear enough. Of course, for both the experiments of Pastoor *et al.* (2008) and these simulations, the difference in drag reduction between actuation at $St = 0.11$ and 0.15 is only $\sim$2 %: relatively insignificant given the differences in end conditions and actuation slot configuration.

The above results were obtained for actuation from all four rear-corner slots: two actuating the flow in a direction perpendicular to the free stream immediately upstream of the separation point (shear-layer actuation), and two on the extremities of the rear face actuating the flow in a direction parallel to the free stream (base actuation). The impact of each pair in isolation was also briefly investigated, to obtain further insights into the drag reduction mechanism. To explore this, extra tests were performed at the optimal actuation frequency ($St_{act} = 0.11$): one with only shear-layer actuation, and one with only base actuation actuation. The results are shown in figure 27(*b*).

Not surprisingly, the shear-layer actuation results in a drag signal locked on at the actuation frequency (as observed in the four slot case). However, this lock-on does not seem to guarantee high drag reduction. DMD reveals the reason: the magnitude of mode *N* is not reduced, resulting in a more disturbed wake and less symmetric vortices being shed.

The base actuation case also produces surprising results. While for the four-slot and shear-layer actuation cases the drag signal locks on to the actuation signal, this does not occur at $C_\mu \leqslant 0.008$ (mode *A* does not appear), but at $C_\mu = 0.016$ new behaviour is observed. The substantial drag reduction for the lower momentum coefficient cases can be attributed to a weakening of mode *N*, with the actuation also attenuating the beading behaviour of the natural flow (where the drag would meander significantly upwards at various times). For the highest momentum case mode *A* appears and the drag signal oscillates at St_{act}, but with a secondary oscillation at $2St_{act}$ also present (see figure 28*a*), producing a double peak in each cycle and a substantially lower drag trough. The test was repeated at higher frequencies, with the same behaviour observed. A DMD analysis shows that this form of actuation leads to a new structure of mode *N*, which is shown in figure 28(*b*). In the pictured snapshot, opposite-signed vorticity is apparent in each shear layer, whereas for all other cases mode *N* features same-signed vortices in each shear layer. This produces an asymmetric diagonal structure downstream and may explain the non-sinusoidal drag signal. It appears that base actuation is very successful at disrupting the natural instability in the wake, especially if enough momentum is supplied.

These results show that, for actuation in the low-frequency range, the shear-layer and base actuation achieve drag reduction through different mechanisms: the shear-layer actuation is more successful at creating synchronous vortices in each shear layer, while the base actuation is more successful at disrupting the natural instability. When combined, it appears that the two mechanisms contribute to each other's success

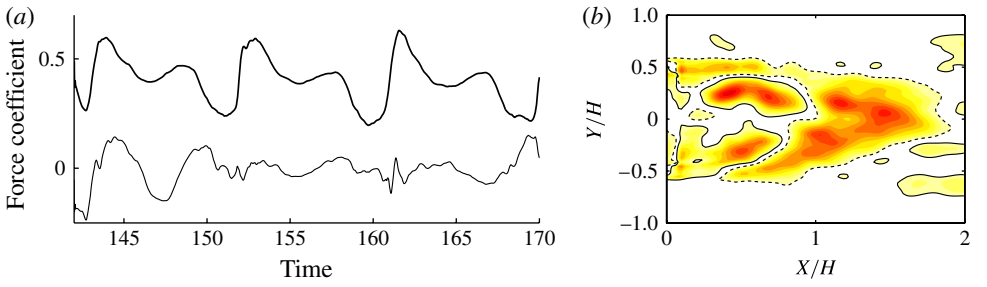

FIGURE 28. (Colour online) (*a*) Drag (thick line) and lift (thin line) signal for base actuation at $St_{act} = 0.11$ and $C_\mu = 0.008$. (*b*) Mode N for the same case as (*a*).

further, as the total drag reduction for four-slot actuation at $C_\mu = 0.008$ is significantly greater than the sum of the drag reduction obtained for shear-layer and base actuation $C_\mu = 0.004$. The momentum coefficient threshold for four-slot actuation, however, does not appear to be the same for shear-layer and base actuation configurations, and the latter may offer the greatest potential for drag reduction provided enough input energy is available. These results also reveal that there may be an optimum angle where actuation from two slots (one on either side) would be most efficient. This is currently being investigated.

4. Conclusion

The numerical approach undertaken in this study has provided new perspectives on the mechanisms involved in open-loop periodic control at the rear of 2D bluff bodies. Focus has been placed on the influence of actuation frequency, with an optimum actuation frequency of $St_{act} = 0.11$ found, slightly lower than the $St_{act} = 0.15$ found experimentally by Pastoor *et al.* (2008), for a similar but not identical setup. Note, however, that the predicted drag reduction at $St_{act} = 0.15$ is only $\sim$2 % less. Increased symmetry of vortex shedding, which leads to a longer formation length, and increased diffusion and cross-annihilation in the near wake, has been observed for all cases of actuation.

Dynamic mode decomposition reveals that the actuation produces an additional mode in the flow, rather than displacing the natural mode. Actuation frequencies in the range $St_{act} = 0.09$–0.135 allow the actuation mode to remain coherent and successfully coexist with the natural mode, while remaining at a high enough frequency to enable the flow to smoothly lock on to actuation. Higher-frequency actuation, while still generating coherent mode A synchronous vortices, has been shown to be less effective due to the lower circulation of the mode A vortices in the near wake, and the difference in their combined effect with mode N vortices. This also helps to explain the success of lower actuation frequencies.

New information on the upstream effect of actuation has also been found, with the stagnation pressure shown to oscillate at the actuation frequency with a lag of approximately 100° for all cases. It has been shown that the strength of this effect is likely amplified by the relatively high blockage ratio.

The influence of shear-layer and base actuation in isolation has been explored, with the findings suggesting that each affects the wake in different ways, and that these mechanisms are beneficial to one another when operating in unison. The base actuation case appears to offer greater potential at this Reynolds number. Further

investigation of these mechanisms is recommended, especially at more practical higher actuation frequencies.

With such a large reliance on forcing the shedding to be predominantly 2D, it remains unclear whether the actuation technique would be as successful for less symmetric scenarios, such as flows over 3D bodies, flows over bodies in ground proximity, and flows over bodies at much higher Reynolds numbers. In terms of the latter two cases, our group is currently extending this study to numerically determine the modifying effects of ground proximity and, through wind tunnel experiments, whether the increased turbulence effects at higher Reynolds numbers decrease the attainable drag reduction.

Acknowledgements

This research was undertaken with the assistance of a computing time grant obtained through the Merit Allocation Scheme of the National Computing Infrastructure (NCI) supported by the Australian Government. D.P. acknowledges financial support for a PhD scholarship through an Australian Research Council (ARC) grant LP0991170.

REFERENCES

AHMED, S. & RAMM, G. 1984 Some salient features of the time averaged ground vehicle wake. *SAE Paper no. 840300*.

BEARMAN, P. W. 1967 The effect of base bleed on the flow behind a two-dimensional model with a blunt trailing edge. *Aeronaut. Q.* **18**, 207–224.

CHIEKH, M. B., MICHARD, M., GUELLOUZ, M. S. & BERA, J. C. 2013 POD analysis of momentumless trailing edge wake using synthetic jet actuation. *Exp. Therm. Fluid Sci.* **46**, 89–102.

COOPER, K. R. 1985 The effect of front-edge rounding and rear-edge shaping on the aerodynamic drag of bluff vehicles in ground proximity. *SAE Technical Paper* 850288.

GERMANO, M., PIOMELLI, U., MOIN, P. & CABOT, W. H. 1991 A dynamic subgrid-scale eddy-viscosity model. *Phys. Fluids* **3** (7), 1760–1765.

GLEZER, A. 2011 Some aspects of aerodynamic flow control using synthetic-jet actuation. *Phil. Trans. R. Soc.* A **369**, 1476–1494.

GRAFTIEAUX, L., MICHARD, M. & GROSJEAN, N. 2001 Combining PIV, POD and vortex identification algorithms for the study of unsteady turbulent swirling flows. *Meas. Sci. Technol.* **12**, 1422–1429.

GRANDEMANGE, M., GOHLKE, M. & CADOT, O. 2013 Turbulent wake past a three-dimensional blunt body. Part 1. Global modes and bi-stability. *J. Fluid Mech.* **722**, 51–84.

HACKETT, J. E., WILSDEN, D. J. & LILLEY, E. E. 1979 Estimation of tunnel blockage from wall pressure signatures: a review and data correlation. *NASA CR* **152**, 241.

HENNING, L., PASTOOR, M., KING, R., NOACK, B. R. & TADMOR, G. 2007 Feedback control applied to the bluff body wake. *Active Flow Control* **95**, 369–390.

HOURIGAN, K., THOMPSON, M. C. & TAN, B. T. 2001 Self-sustained oscillations in flows around long blunt plates. *J. Fluids Struct.* **15**, 387–398.

HSU, T. Y., HAMMACHE, M. & BROWAND, F. 2002 Base flaps and oscillatory perturbations to decrease base drag. In *The Aerodynamics of Heavy Vehicles: Trucks, Buses, and Trains*, vol. 1, pp. 303–316. Springer.

HUERRE, P. & MONKEWITZ, P. 1990 Local and global instabilities in spatially developing flows. *Annu. Rev. Fluid Mech.* **22**, 473–537.

KRAJNOVIC, S. 2009 Large eddy simulation of flows around ground vehicles and other bluff bodies. *Phil. Trans. R Soc.* A **367**, 2917–2930.

KRAJNOVIC, S. & FERNANDES, J. 2011 Numerical simulation of the flow around a simplified vehicle model with active flow control. *Intl J. Heat and Fluid Flow* **32**, 192–200.

LEHMKUHL, O., RODRÍGUEZ, I., BORRELL, R., PÉREZ-SEGARRA, C. D. & OLIVA, A. 2011 Low-frequency variations in the wake of a circular cylinder at $Re = 3900$. *J. Phys.: Conf. Ser.* **318**, 042038.

LILLY, D. K. 1992 A proposed modification of the Germano subgrid-scale closure method. *Phys. Fluids* A **4** (3), 633–635.

MERCKER, E. 1986 A blockage correction for automotive testing in a wind tunnel with closed test section. *J. Wind Engng & Indust. Aerodyn* **22**, 149–167.

MEZIC, I. 2013 Analysis of fluid flows via spectral properties of the Koopman operator. *Annu. Rev. Fluid Mech.* **45**, 357–378.

MILLS, R., SHERIDAN, J. & HOURIGAN, K. 2001 Response of base suction and vortex shedding from rectangular prisms to transverse forcing. *J. Fluid Mech.* **461**, 25–49.

NISHRI, B. & WYGNANSKI, I. 1998 Effects of periodic excitation on turbulent flow separation from a flap. *AIAA J.* **36** (4), 547–556.

PARK, H., LEE, D., JEON, W., HAHN, S. & KIM, J. 2006 Drag reduction in flow over a two-dimensional bluff body with a blunt trailing edge using a new passive device. *J. Fluid Mech.* **563**, 389–414.

PASTOOR, M., HENNING, L., NOACK, B. R., KING, R. & TADMOR, G. 2008 Feedback shear layer control for bluff body drag reduction. *J. Fluid Mech.* **608**, 161–196.

PETRUSMA, M. S. & GAI, S. L. 1994 The effect of geometry on the base pressure recovery of the segmented blunt trailing edge. *Aeronaut. J.* **98**, 267–274.

ROCKWELL, D. & NAUDASCHER, E. 1979 Self-sustained oscillations of impinging free shear layers. *Annu. Rev. Fluid Mech.* **11**, 67–94.

RODRIGUEZ, O. 1991 Base drag reduction by the control of three-dimensional unsteady vortical structures. *Exp. Fluids* **11**, 218–226.

ROWLEY, C. W., MEZIC, I., BAGHERI, S., SCHLATTER, P. & HENNINGSON, D. S. 2009 Spectral analysis of nonlinear flows. *J. Fluid Mech.* **641**, 115–127.

SCHMID, P. J. 2010 Dynamic mode decomposition of numerical and experimental data. *J. Fluid Mech.* **656**, 5–28.

SCHMID, P. J. 2011 Application of the dynamic mode decomposition to experimental data. *Exp. Fluids* **50**, 1123–1130.

SCOTTI, A., MENEVEAU, C. & FATICA, M. 1997 Dynamic Smagorinsky model on anisotropic grids. *Phys. Fluids* **9** (6), 1856–1858.

TANNER, M. 1972 A method of reducing the base drag of wings with blunt trailing edges. *Aeronaut. J.* **23**, 15–23.

TOMBAZIS, N. & BEARMAN, P. W. 1997 A study of three-dimensional aspects of vortex shedding from a bluff body with a mild geometric disturbance. *J. Fluid Mech.* **330**, 85–112.